

1 **IGHV3-53 antibody abundance drives divergent SARS-CoV-2 immune imprinting**

2 Xiao Niu^{1,2,3,#}, Fanchong Jian^{1,#}, Yutong Li^{1,2}, Ke Li^{1,2}, Siyu Lei^{1,2,4}, Weiliang Song^{1,2}, Ruoxi Kong^{1,2},
3 Xingan Cai^{1,2}, Ran An², Yao Wang², Yifei Huang^{5,6,7}, Lingling Yu², Wenjing Wang², Haiyan Sun²,
4 Yuanling Yu², Jing Wang², Binmao Zhang⁸, Tianen Zhu^{8,9}, Jianheng Huang^{8,10}, Fei Shao², Xiaotian
5 Tan⁸, Sai Luo^{5,6,7}, Yunlong Cao^{1,2,4*}

6 ¹Biomedical Pioneering Innovation Center (BIOPIC), School of Life Sciences, Peking University,
7 Beijing, P.R. China.

8 ²Changping Laboratory, Beijing, P.R. China.

9 ³College of Chemistry and Molecular Engineering, Peking University, Beijing, P.R. China.

10 ⁴Peking–Tsinghua Center for Life Sciences, Peking University, Beijing, P. R. China.

11 ⁵Center for Infectious Disease Research, Tsinghua University, Beijing, P.R. China.

12 ⁶Tsinghua-Peking Joint Center for Life Sciences, Tsinghua University, Beijing, P.R. China.

13 ⁷School of Basic Medical Sciences, Tsinghua University, Beijing, P.R. China.

14 ⁸Shenzhen Institutes of Advanced Technology, Chinese Academy of Sciences.

15 ⁹Shenzhen University General Hospital.

16 ¹⁰Shenzhen University.

17 *Correspondence: Yunlong Cao (yunlongcao@pku.edu.cn).

18 #These authors contributed equally.

19

20 **Abstract**

21 The mechanisms driving divergent SARS-CoV-2 immune imprinting in populations primed with
22 different COVID-19 vaccines remain unclear. Recipients of inactivated vaccines readily develop
23 Omicron-specific antibodies through repeated breakthrough infections, whereas mRNA-vaccinated
24 individuals exhibit severe ancestral-strain imprinting that suppresses *de novo* Omicron-specific
25 responses. These differences could result in distinct antibody landscapes, leading to regional
26 epidemiological divergence and necessitating region-specific vaccine update strategies. Importantly,
27 conventional wild-type mouse models fail to recapitulate strong human SARS-CoV-2 imprinting,
28 which significantly hinders imprinting-related mechanistic investigation and vaccine update
29 evaluation. Here, we surprisingly found that V(D)J-humanized mice could faithfully recapitulate
30 human severe SARS-CoV-2 immune imprinting phenotypes. Comprehensive antibody repertoire
31 and epitope mapping of 583 monoclonal antibodies from these models revealed that the abundance
32 of pre-existing human IGHV3-53/66-encoded SARS-CoV-2 antibody responses determine
33 imprinting severity following Omicron exposure through antibody-mediated masking of Omicron-
34 specific epitopes. Both passive transfer of IGHV3-53/66 antibodies and knock-in of the human
35 IGHV3-53 gene were sufficient to induce severe SARS-CoV-2 imprinting in wild-type mice.
36 Concordantly, head-to-head comparison also showed that mRNA vaccine recipients retained higher
37 IGHV3-53/66 antibody abundance and thus stronger imprinting than inactivated vaccine recipients.
38 Consequently, compared to NB.1.8.1, XFG exhibits greater immune evasion in mRNA-vaccinated
39 individuals but not in inactivated vaccine recipients. This explains the regional predominance of
40 XFG in mRNA-vaccinated populations, while NB.1.8.1 prevails in inactivated vaccine-dominated
41 countries. Together, these findings demonstrate that the V(D)J germline repertoire—even a single
42 germline-encoded antibody response—can profoundly shape humoral imprinting severity.
43 Accordingly, we constructed a human IGHV3-53 knock-in mouse model that can accurately
44 recapitulate human SARS-CoV-2 antibody landscape, providing a valuable tool for guiding future
45 COVID-19 vaccine updates.

47 **Main**

48 Extensive studies have investigated immune imprinting in SARS-CoV-2 ¹, yet the reasons why
49 different vaccine platforms produce markedly different imprinting severity have remained unclear.
50 Recipients of mRNA vaccines exhibit pronounced immune imprinting, persistently recalling
51 ancestral Wuhan-Hu-1 (Wuhan) spike-reactive antibodies even upon repeated Omicron exposures,
52 significantly limiting the development of Omicron-specific neutralizing responses ²⁻¹⁰. In contrast,
53 individuals only receiving inactivated vaccines, predominantly in China, demonstrate greater
54 adaptability in humoral responses, developing robust Omicron-specific antibodies upon repeated
55 infections or boosters, thus overriding Wuhan immune imprinting ¹¹⁻¹⁴.

56 This distinct imprinting pattern has become increasingly consequential, as it aligns with the
57 emerging global divergence in SARS-CoV-2 epidemiology: the XFG lineage currently leads in areas
58 with high mRNA vaccine coverage, whereas NB.1.8.1 is dominant in nations that primarily used
59 inactivated vaccines, especially in China ([Extended Data Fig. 1a](#)) ¹⁵⁻²⁰.

60 Understanding the mechanistic basis of this imprinting divergence is critical, not only because it
61 may have directly influenced real-world viral epidemiology—potentially necessitating region-
62 specific vaccine update strategies—but also because these distinct imprinting phenotypes provide a
63 unique opportunity to uncover general principles of humoral immune imprinting applicable to other
64 pathogens, such as influenza.

65 However, direct head-to-head comparisons of imprinting severity and antibody repertoires between
66 mRNA- and inactivated-vaccine recipients have been limited by challenges in sample collection
67 and international sample shipping. Moreover, conventional wild-type mouse models fail to
68 recapitulate the strong imprinting observed in humans ^{2,11,13}, severely hindering mechanistic studies
69 and preclinical evaluation of SARS-CoV-2 vaccines.

70 In this paper, we present a head-to-head comparison of antibody repertoires, imprinting severity,
71 and responses to emerging variants in individuals primed with mRNA versus inactivated vaccines.
72 These analyses reveal that differences in immune imprinting are already influencing real-world
73 epidemiology, contributing to the distinct regional dominance of XFG and NB.1.8.1. Using V(D)J-
74 humanized mice, we demonstrate faithful recapitulation of strong human-like imprinting and

75 identify pre-existing human IGHV3-53/66-encoded antibodies as the key driver of imprinting
76 severity via epitope masking. Finally, we establish a human IGHV3-53 knock-in mice model that
77 accurately recapitulate human SARS-CoV-2 antibody responses, offering a practical tool for
78 evaluating future vaccine update strategies.

79

80 **Distinct immune imprinting in humans**

81 To directly compare the humoral immunity in individuals primed with mRNA versus inactivated
82 vaccines, we recruited 20 participants stratified into two cohorts based on vaccination history
83 ([Supplementary Table 1](#) and [Fig. 1a](#)). Despite the modest sample size, these cohorts present a rare
84 opportunity to directly compare mRNA and inactivated vaccine priming outcomes. All participants
85 had resided in the same region since 2021 and had experienced multiple Omicron infections. The
86 inactivated-only cohort (n = 12) received three doses of CoronaVac, with samples collected $46.5 \pm$
87 5.4 months after the first vaccine dose. The mRNA-vaccinated cohort (n = 8) received at least one
88 mRNA vaccine dose (BNT162b2 or mRNA-1273), with samples collected 46.0 ± 2.3 months after
89 initial vaccination. Although detailed infection histories were unavailable, widespread Omicron
90 transmission following China's reopening strongly suggests that most participants were exposed to
91 at least BA.5 and JN.1 sublineages.

92 To assess immune imprinting, we first used fluorescence-activated cell sorting (FACS) to quantify
93 cross-reactive memory B cells, defined as the proportion of Wuhan⁺ cells among JN.1⁺ memory B
94 cells ([Fig. 1b](#) and [Supplementary Information Fig. 1a](#)). The mRNA-vaccinated cohort indeed
95 exhibited a significantly higher proportion of cross-reactive memory B cells than the inactivated-
96 only cohort, indicating stronger imprinting ([Fig. 1c](#)). Additionally, the mRNA-vaccinated group
97 showed a higher proportion of Wuhan⁺ memory B cells, reflecting persistent responses to the
98 ancestral strain. In contrast, JN.1⁺ memory B cell frequencies were comparable between groups,
99 suggesting comparable responses to recent variants despite different priming histories ([Fig. 1c](#)).

100 To examine antibody specificity, we depleted Wuhan RBD-binding antibodies from serum and
101 measured the remaining IgG titres against the JN.1 RBD ([Fig. 1d](#)). This depletion nearly abolished
102 JN.1-binding activity in the mRNA-vaccinated cohort (23-fold reduction), indicating that the

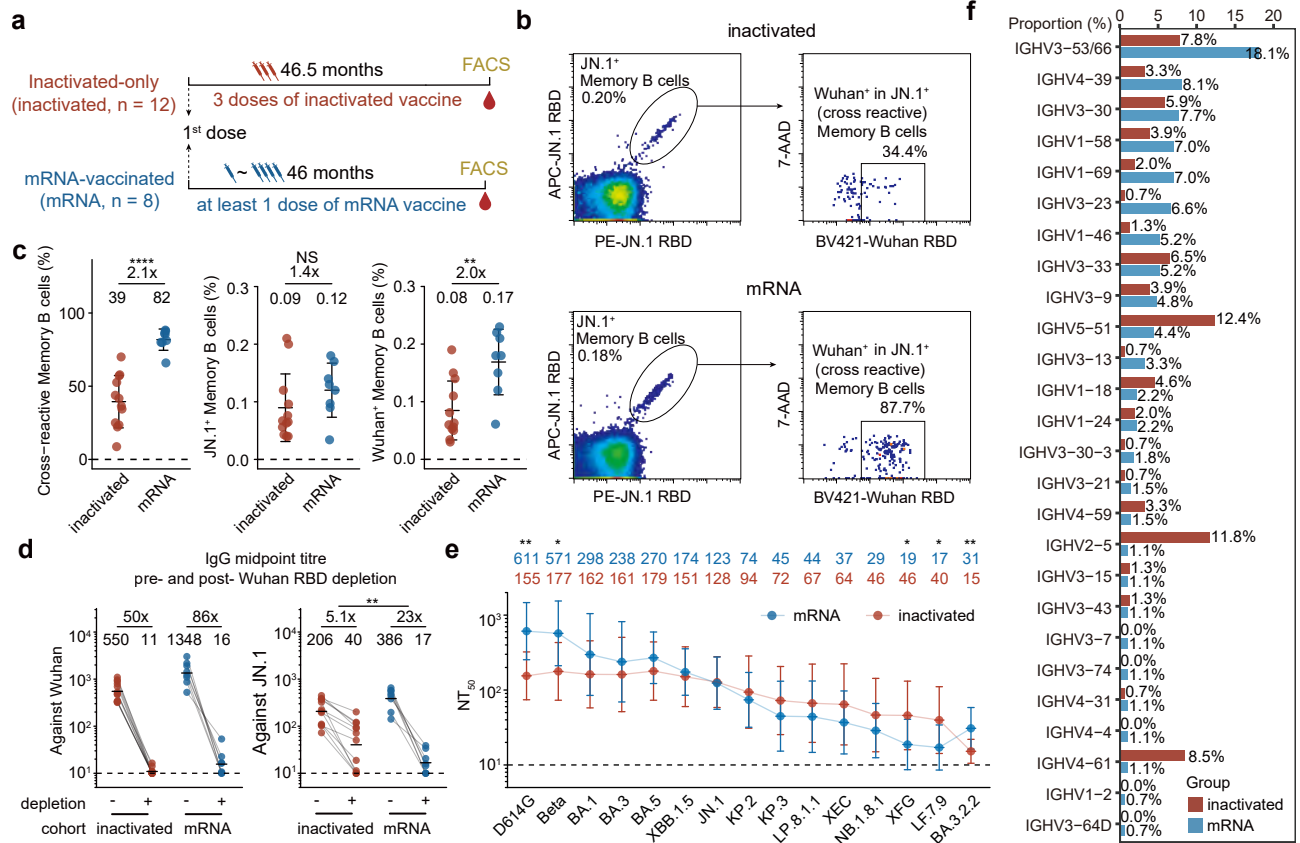


Figure 1 | mRNA and inactivated vaccine priming induce distinct levels of immune imprinting.

a, Schematic of the SARS-CoV-2-related immune histories and sampling time of the inactivated-only and mRNA-vaccinated cohorts involved in this study. **b**, Representative flow cytometry dot plots of cross-reactive memory B cells from individuals from the inactivated-only (top) and mRNA-vaccinated (bottom) cohorts. APC, allophycocyanin; PE, phycoerythrin; BV421, Brilliant Violet 421. **c**, Scatter plots showing the proportion of cross-reactive memory B cells (left), JN.1-reactive memory B cells (middle), and Wuhan-reactive memory B cells (right). **d**, Serum IgG midpoint titre against Wuhan (left) or JN.1 (right) RBD before and after Wuhan RBD depletion. Statistical significance of the fold-reduction in titres was assessed between two cohorts. Dashed lines indicate the limit of detection (midpoint titre = 10). **e**, NAb response of the two cohorts against a panel of SARS-CoV-2 variant pseudoviruses. Geometric mean titres (GMTs) are shown on the top. Dashed lines indicate the limit of detection ($NT_{50} = 10$). **f**, Frequency of heavy chain V gene usage proportion of the two cohorts. IGHV3-53 and IGHV3-66 were combined for analysis. Two-tailed Wilcoxon rank-sum tests were used in c-e. * $P < 0.05$, ** $P < 0.01$, *** $P < 0.001$, **** $P < 0.0001$; NS, not significant ($P > 0.05$).

103 response was almost entirely contributed by cross-reactive antibodies. In contrast, the inactivated-
104 only cohort showed a more modest decrease (5.1-fold), consistent with the presence of a subset of
105 JN.1-specific antibodies (Fig. 1d).

106 Neutralization assays against a pseudovirus panel further supported this divergence (Fig. 1e). In the
107 mRNA-vaccinated cohort, 50% neutralization titres (NT₅₀) were highest for D614G and declined
108 rapidly with newer variants^{21–25}. In contrast, the inactivated-only cohort maintained relatively stable
109 neutralization, declining only from JN.1 onward^{11,13,17,26–29}. Interestingly, the NT₅₀ curves
110 intersected at JN.1, beyond which the inactivated-only cohort showed higher neutralization. These
111 data suggest that, owing to stronger immune imprinting, the mRNA-vaccinated cohort's
112 neutralizing responses to emerging variants are strongly confined by the recall and expansion of
113 antibodies originally elicited by ancestral exposure, whereas the more adaptable response in the
114 inactivated-only cohort enables superior neutralization of later-emerging variants.

115 Notably, the mRNA-vaccinated cohort showed a marked reduction in titres against XFG relative to
116 NB.1.8.1, whereas the inactivated-only cohort displayed comparable neutralizing activity against
117 both variants. This disparity provides a serological explanation for the regional predominance of
118 XFG in mRNA-vaccinated populations and NB.1.8.1 in inactivated vaccine-dominated countries¹⁷.
119 Additionally, neutralization titres against BA.3.2.2 were significantly higher in the mRNA-
120 vaccinated cohort (Fig. 1e). This variant carries unique mutations that have been shown to evade
121 Class 1/4 antibodies prevalent in inactivated vaccinees but not the dominant Class 1 antibodies
122 induced by mRNA vaccines¹⁷. Collectively, these head-to-head comparisons of serological and flow
123 cytometry data confirm robust imprinting in the mRNA-vaccinated cohort and weaker imprinting
124 in the inactivated-only cohort that can be partially overcome. Such imprinting differences have
125 resulted in distinct antibody landscapes, contributing to regional epidemiological divergence and
126 raising the potential necessity for region-specific vaccine update strategies.

127 While the lack of longitudinal samples makes it challenging to trace the evolutionary mechanism of
128 this divergence in humans, distinct signatures within the BCR repertoire may offer critical insights.
129 To explore these correlates, we performed plate-based single B cell V(D)J sequencing to compare
130 heavy-chain V-gene usage of JN.1⁺ memory B cells between the two cohorts (Fig. 1f)³⁰. The
131 mRNA-vaccinated cohort showed enriched usage of IGHV3-53/66—germline genes encoding

132 "public" antibodies targeting the Class 1 epitope, which overlaps with the ACE2-binding site ^{31–38}.
133 These neutralizing antibodies are broadly elicited by Wuhan vaccination or infection and are well
134 known for their potent neutralizing capacity ^{31,37}. In contrast, the inactivated-only cohort showed
135 greater representation of IGHV5-51 and IGHV2-5, associated with Omicron-specific Class 1/4
136 antibodies ²⁶. The differences in light chain V-gene usage between the two cohorts were less
137 pronounced, with both groups showing a preference for IGKV1-39, IGKV3-20, and IGKV1-33
138 ([Extended Data Fig. 2a](#)).

139 These findings suggest that the IGHV3-53/66–encoded Class 1 antibodies—originally elicited by
140 ancestral Wuhan strain exposure—are preferentially recalled and expanded upon repeated Omicron
141 encounters, and the mRNA-vaccinated cohort exhibits much higher IGHV3-53/66 antibody
142 abundance compared to the inactivated-only cohort, due to its higher priming vaccine
143 immunogenicity. Although our analysis was limited by small cohort sizes and unavoidable
144 demographic heterogeneity (e.g., age, sex, and infection history), the observed immune imprinting
145 patterns align remarkably well with extensive prior studies ^{2–9,11–14}. Importantly, this parallel
146 analysis enabled us to observe a correlation between IGHV3-53/66-encoded SARS-CoV-2 antibody
147 enrichment and imprinting severity. To move beyond correlation and rigorously establish causality,
148 it is critical to establish a animal model that can control strictly matched immune histories while
149 faithfully recapitulating the severe immune imprinting observed in human mRNA vaccinees.

150

151 **V(D)J-humanized mice mimic strong imprinting**

152 Previous studies have shown that wild-type mice do not recapitulate the strong SARS-CoV-2
153 immune imprinting observed in the human mRNA-vaccinated cohort ². Given that our human data
154 identified a critical role for the IGHV3-53/66 germline genes in severe SARS-CoV-2 imprinting,
155 we hypothesized that the absence of these specific human V-genes in the murine repertoire explains
156 this discrepancy. Therefore, we employed V(D)J humanized mice for comparative analysis. These
157 BALB/c-derived mice, commonly used in therapeutic antibody discovery, carry human
158 immunoglobulin V(D)J genes for all heavy chains and kappa light chains ([Supplementary
159 Information Fig. 4a](#)). Both V(D)J humanized and wild-type mice were primed with three doses of

Figure 2

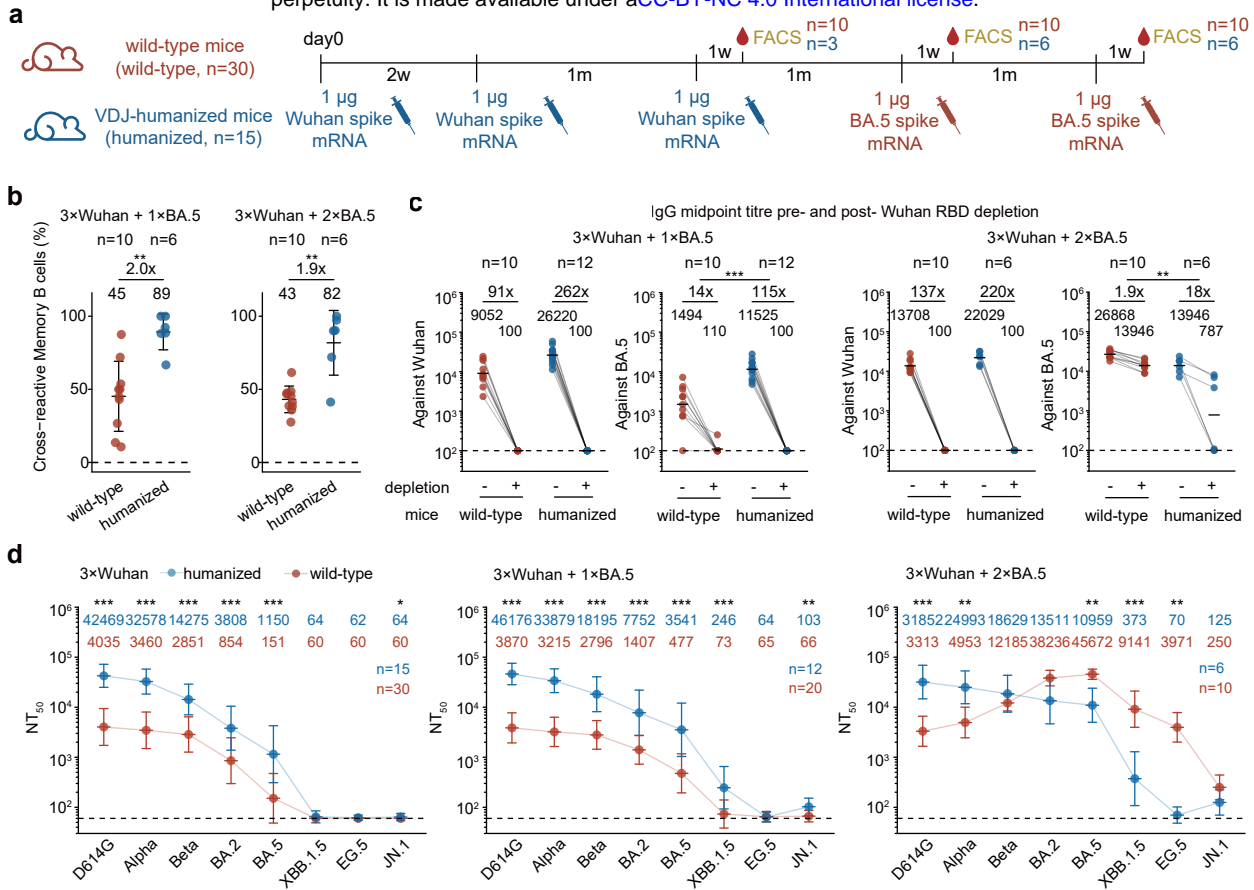


Figure 2 | V(D)J-humanized mice recapitulate severe SARS-CoV-2 imprinting.

a, Schematic of the mouse immunization regimen and sampling timeline for wild-type and V(D)J-humanized mice. The number of mice is indicated at the time point for each endpoint experiment. b, Scatter plots showing the proportion of cross-reactive memory B cells in draining lymph nodes of the two mouse strains after one (left) or two (right) BA.5 boosts. c, Serum IgG midpoint titre of the two mouse strains after one (left) or two (right) BA.5 boosts against Wuhan or BA.5 RBD before and after Wuhan RBD depletion. Statistical significance of the fold-reduction in titres was assessed between humanized and wild-type mice. Dashed lines indicate the limit of detection (midpoint titre = 100). d, Serum neutralization titres (NT_{50}) of the two mouse models after Wuhan priming (left), one BA.5 boost (middle), or two BA.5 boosts (right) against a panel of SARS-CoV-2 variant pseudoviruses. Geometric mean titres (GMTs) are shown on the top. Dashed lines indicate the limit of detection ($NT_{50} = 60$). Two-tailed Wilcoxon rank-sum tests were used in b-d.

160 ancestral mRNA vaccine (encoding the spike protein of SARS-CoV-2 ancestral strain), followed by
161 two booster doses of BA.5 mRNA vaccine to mimic human exposure history to SARS-CoV-2
162 variants (Fig. 2a). Blood, spleens, and lymph nodes were collected one week after the third ancestral
163 dose and each BA.5 dose for serological and flow cytometry analyses.

164 We first performed FACS analysis on mouse lymph nodes to assess cross-reactivity among memory
165 B cells and germinal-center (GC) B cells (Supplementary Information Fig. 1b). As expected, wild-
166 type mice harbored abundant BA.5-specific memory and GC B cells after each BA.5 booster (Fig.
167 2b and Extended Data Fig. 3a). In striking contrast, the V(D)J-humanized mice exhibited a strong
168 imprinting phenotype, developing a high proportion of cross-reactive memory B cells (89% and 82%
169 after the first and second boosters, respectively) that mirrored the response observed in the human
170 mRNA-vaccinated cohort. Despite similar overall percentages of GC B cells, humanized mice
171 showed a significantly higher frequency of cross-reactive GC B cells after one BA.5 booster,
172 indicating that their GC response was dominated by Wuhan-strain imprinted B cells (Extended Data
173 Fig. 3a and 3b). Additionally, they presented a significantly higher frequency of class-switched
174 memory B cells, which aligns with the preferential recall and expansion of a pre-existing memory
175 population typical of immune imprinting (Extended Data Fig. 3c).

176 The imprinting was also faithfully reflected in the serological response. Wuhan RBD-depletion
177 caused a substantially greater drop in BA.5-binding IgG titres in humanized mice than in wild-type
178 mice (18-fold vs. 1.9-fold), although the magnitude of this effect varied among individual
179 humanized mice (Fig. 2c). Specifically, titres in three humanized mice dropped to undetectable
180 levels, while the remaining three exhibited modest reductions. The post-depletion titre ratio was
181 inversely correlated with the proportion of cross-reactive memory B cells (Supplementary
182 Information Fig. 3a), demonstrating consistency between cellular and serological assays and
183 reflecting individual heterogeneity in imprinting strength.

184 We next compared serum neutralization profiles between the two mouse models (Fig. 2d and
185 Extended Data Fig. 4a). Initially, following Wuhan priming, humanized mice mounted a
186 significantly more potent and broad response than wild-type mice. Two BA.5 boosters successfully
187 shifted the neutralizing antibody (NAb) preferences of wild-type mice toward Omicron variants. In
188 contrast, the neutralization curves of humanized mice closely mirrored those of the mRNA-

189 vaccinated cohort, with titres remaining maximal against D614G despite repeated Omicron
190 exposure, indicating strong immune imprinting that could not be overcome by two doses of BA.5
191 boosting ([Extended Data Fig. 4a](#)). Together, these data collectively demonstrate that humanized
192 mice can mirror SARS-CoV-2 imprinting. This divergence between the two mouse models strongly
193 suggests that the presence of human immunoglobulin V(D)J genes is a critical determinant of the
194 imprinting phenotype.

195

196 **Distinct antibody landscapes of mouse models**

197 To dissect the molecular basis of imprinting, we tracked the evolution of antibody repertoire from
198 the two mouse models throughout Wuhan-priming and BA.5-boosting. We sorted RBD-specific
199 memory B cells from spleens of humanized and wild-type mice following Wuhan priming (sorted
200 on Wuhan RBD) and after each BA.5 booster (sorted on BA.5 RBD; [Supplementary Information](#)
201 [Fig. 1c](#)). Single-cell V(D)J sequencing of paired heavy- and light-chain variable regions generated
202 583 unique monoclonal antibodies (mAbs) from the six mice groups. These mAbs were
203 recombinantly expressed as human IgG1 ([Supplementary Table 2](#)), and their half-maximal
204 inhibitory concentration (IC₅₀) measured via pseudovirus neutralization assay ([Extended Data Fig.](#)
205 [5a](#)). Consistent with the established imprinting signature, enzyme-linked immunosorbent assay
206 (ELISA) revealed that antibodies from humanized mice exhibited a higher proportion of cross-
207 reactivity than those from wild-type mice ([Extended Data Fig. 5b](#)).

208 To systematically dissect the divergence in antibody epitope distribution between humanized and
209 wild-type mice, we employed high-throughput yeast-display-based deep mutational scanning (DMS)
210 to map the RBD mutations that could escape the isolated mAbs and define the epitope targeted
211 ^{13,26,39–41}. We built single-site saturation mutant libraries based on the Wuhan-Hu-1 and BA.5 RBDs
212 and performed DMS for antibodies isolated following Wuhan priming or BA.5 boosting,
213 respectively. The resulting escape profiles of 583 mAbs define the critical residues that mediate
214 immune evasion and facilitating their precise categorization into distinct epitope clusters.

215 IC₅₀-weighted escape profiles show that neutralizing antibodies from wild-type and humanized mice
216 exhibit distinct escape hotspot sites ([Fig. 3a-3c](#) and [Extended Data Fig. 6a-6c](#)). Following Wuhan

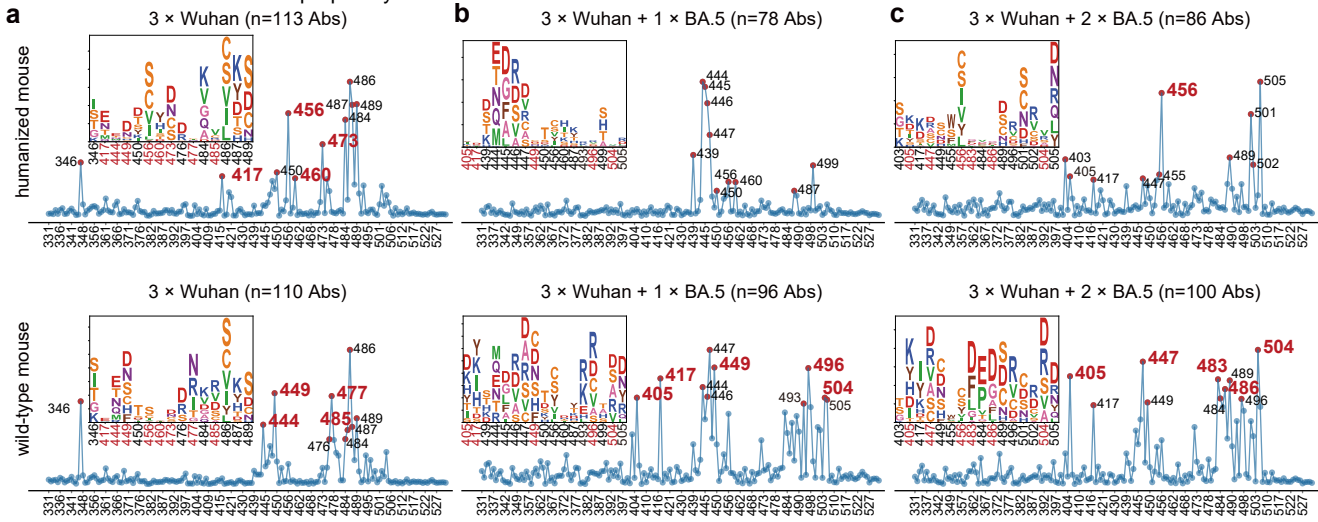


Figure 3 | Distinct antibody landscapes between mRNA vaccinated humanized and wild-type mice.

a–c. Normalized average DMS escape scores for mAbs isolated from humanized (top) and wild-type mice (bottom) following Wuhan priming (a), the first BA.5 booster (b), or the second BA.5 booster (c). Escape scores were aggregated and weighted by the IC_{50} of each individual mAb (To focus on the neutralizing mAbs, lower IC_{50} corresponds to greater weight) against D614G for Wuhan-primed groups or BA.5 for BA.5-boostered groups. Codon constraints were applied (see Methods). In each panel, the ten residues with the highest cumulative escape scores are annotated, with their specific mutational escape profiles visualized as logo plots above the scatter plots. To highlight divergent immune pressure, residues exhibiting pronounced differences between humanized and wild-type strains (as identified in Extended Data Fig. 6) are colored red in both the scatter plots and logo plots.

217 priming, the NAb elicited in humanized mice substantially focused on Class 1 epitopes, featured
218 by hotspots at residues 417, 456, 460, and 473. Although wild-type mice displayed a comparable
219 landscape after Wuhan priming, they lacked these Class 1 peaks, instead featuring residue 477 as a
220 characteristic hotspot (Fig. 3a). BA.5 boosting leads to further divergence between the two mouse
221 models. In humanized mice, the prominent Class 1 hotspots (e.g., residue 456) persisted obstinately
222 throughout the boosting regimen. In contrast, the wild-type repertoire diverged significantly upon
223 boosting, characterized by the emergence of distinct Class 1/4 escape peaks, such as residue 504
224 (Fig. 3b-3c).

225 To translate these differences in escape sites into a more intuitive view of epitope-level repertoire
226 differences, we categorized the 583 mAbs into 9 epitope groups (Supplementary Information Fig.
227 2a)¹³. Names of the epitope groups were generally assigned in line with the epitope groups on
228 Wuhan RBD defined previously^{42,43}. We then comprehensively analyzed the antibody repertoires
229 elicited in humanized and wild-type mice after each timepoint (Fig. 4a and 4b, Extended Data Fig.
230 7a-7d). Following Wuhan priming, humanized mice uniquely elicited a dominant population of
231 antibodies targeting the A1 epitope (Fig. 4a). Notably, antibodies targeting this epitope are closely
232 related to the IGHV3-53 germline and target key residues such as 456, aligning with the escape
233 hotspots. The foundational divergence between the two mouse models was established immediately
234 after Wuhan priming. After two BA.5 boosting doses, while dynamic shifts occurred—including the
235 abrogation of Group B and the emergence of Group A2—the A1 response remained persistent in
236 humanized mice but was completely absent in wild-type mice (Fig. 4c and Extended Data Fig. 7a
237 and 7c). In contrast, Omicron-specific antibodies in epitope groups B, D, and F3 contribute mostly
238 to the neutralization against BA.5 exclusively in wild-type but not the V(D)J-humanized mice.

239 Overall, DMS analysis demonstrates that Class 1 (A1) antibodies should play a pivotal role in the
240 response to Wuhan priming, serving as a defining characteristic of the V(D)J-humanized mouse
241 model, compared to the wild-type mice. This antibody subset substantially contributed to the
242 polyclonal neutralization landscape and could be robustly recalled upon BA.5 boosting. Notably,
243 these A1 antibodies exhibited remarkable germline convergence, consistently dominated by
244 IGHV3-53 after both Wuhan priming and subsequent BA.5 boosting (Fig. 4a). This mirrors the
245 IGHV3-53/3-66 dominance observed in human mRNA-vaccinated cohort. Collectively, these

Figure 4

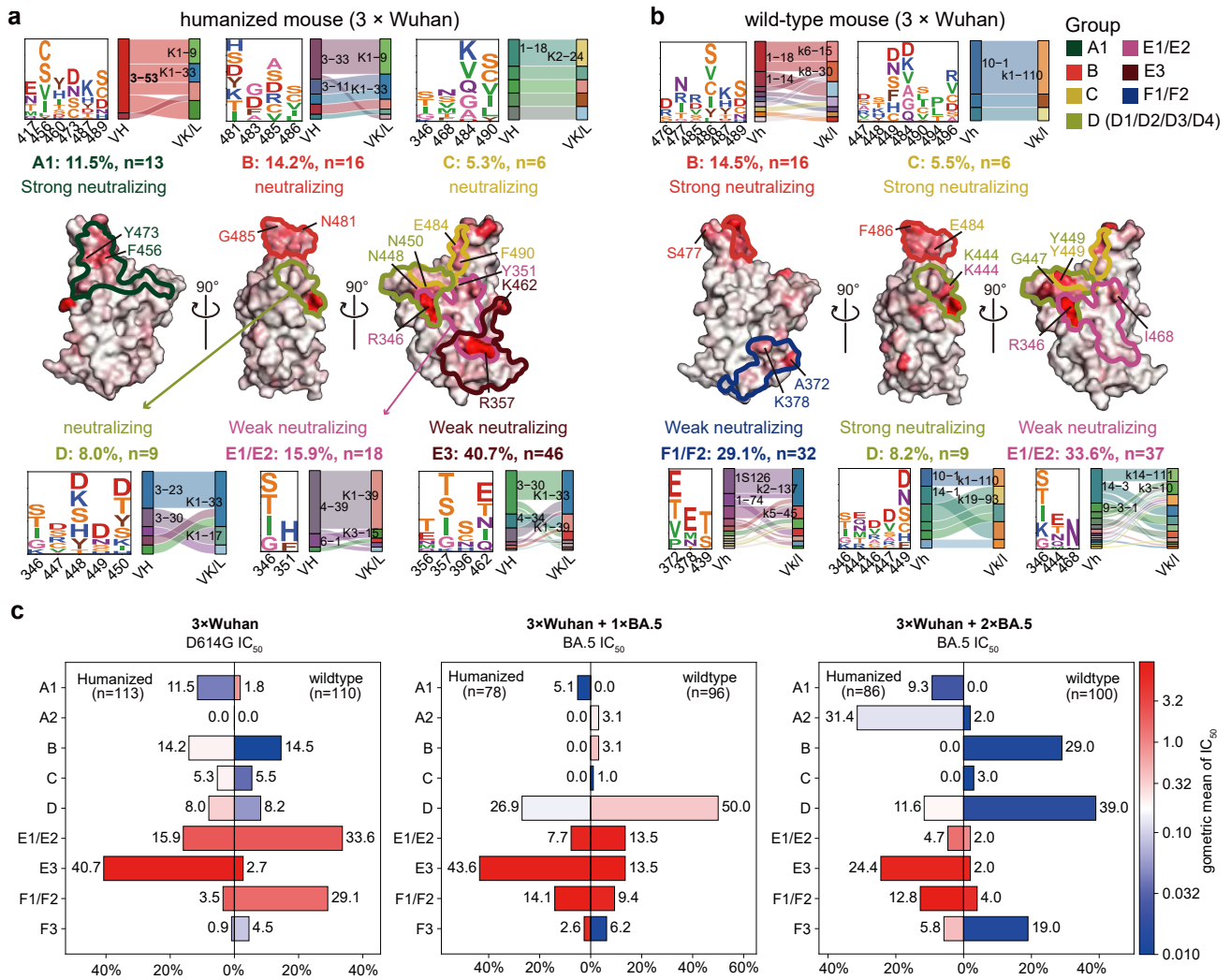


Figure 4 | V(D)J germline difference shapes vaccination-induced SARS-CoV-2 antibody epitope distribution.

Epitope distribution of the antibody repertoire generated after Wuhan priming in humanized (a) and wild-type mice (b). The Wuhan RBD structure (PDB: 6m0j) is displayed as a surface map colored by normalized aggregate escape scores, with major epitope groups outlined in distinct colors. Their neutralizing category, antibody count, and percentage are indicated. Neutralizing category is classified based on geometric mean of IC₅₀: Strong neutralizing (<0.1 μg/mL), Neutralizing (0.1 ≤ IC₅₀ < 1 μg/mL), and Weak neutralizing (1 ≤ IC₅₀ ≤ 10 μg/mL). Epitope groups accounting for <5% of the total antibodies are not labeled. Key escape residues for each group are displayed as logos, and the sites with the highest escape scores per group are labeled on the structure. Paired heavy and light chain V-gene usage for each epitope is shown in Sankey plots. c, Pyramidal bar charts showing the proportional distribution of epitope groups in antibodies isolated from humanized and wild-type mice after Wuhan priming and after one or two BA.5 boosts. Bars are colored according to the log₁₀ geometric mean IC₅₀ of antibodies within each group.

246 findings led us to hypothesize that the dominant, IGHV3-53/66-driven A1 antibody response
247 induced by Wuhan priming is the mechanistic driver of SARS-CoV-2 immune imprinting.

248

249 **Molecular mechanism of imprinting**

250 Given that immune imprinting relies on the recall of pre-existing memory B cells, we then confirmed
251 the cross-reactivity of these IGHV3-53/66-encoded A1 antibodies to determine their potential for
252 reactivation by the Omicron booster (Fig. 5a). 38% of A1 mAbs from Wuhan-primed humanized
253 mice were cross-reactive, constituting a pre-existing memory pool that was efficiently recalled to
254 achieve 100% cross-reactivity upon BA.5 boosting. In contrast, the negligible A1 response in
255 primed wild-type mice was entirely Wuhan-specific and thus completely escaped by BA.5, resulting
256 in the total absence of A1 antibodies following the boosters. Competitive SPR mapping revealed
257 that A1 antibodies compete with ACE2 and the majority of antibodies targeting neutralizing epitopes
258 (A2, B, C, D4, F3). Conversely, they showed minimal to no competition with Group D1 or the
259 weakly or non-neutralizing E and F antibodies (Fig. 5b).

260 These results indicate that A1 antibodies can sterically mask most other major neutralizing sites on
261 Omicron RBD from access by other antibodies and their corresponding B cell receptors. Enabled
262 by the IGHV3-53/66 germline genes, Wuhan priming induces a high-frequency pool of these potent
263 "masking" antibodies, the abundance of which scales directly with the intensity of the priming.
264 Critically, a significant portion of this pool is not escaped by Omicron and remains cross-reactive,
265 making it available for recall upon subsequent Omicron exposure. Therefore, during Omicron
266 vaccination, this pre-existing and cross-reactive memory B cell population is preferentially
267 reactivated and expanded. Such a potent, recalled response could actively outcompete and suppress
268 the *de novo* activation of B cells targeting novel Omicron-specific epitopes by antibody masking,
269 providing a direct mechanistic basis for the strong immune imprinting observed in humanized mice.
270 (Fig. 5c).

271 To test whether these antibodies can indeed drive strong imprinting *in vivo*, we performed passive
272 antibody transfer experiments in wild-type mice (Fig. 5d). Wuhan-primed wild-type mice were
273 infused with BD55-1205 (a representative IGHV3-66-encoded A1 broad neutralizing antibody ⁴⁴)

Figure 5



Figure 5 | IGHV3-53/66-encoded Class 1 antibody drives SARS-CoV-2 imprinting through epitope masking.

a, Donut plots showing the cross-reactivity of A1 antibodies from humanized or wild-type mice. The number of antibodies are indicated in the centre of the donut. Antibodies exhibiting ELISA OD450 values > 2 against both WT and BA.5 RBDs (1 µg/mL) were defined as cross-reactive. Those showing an OD450 > 2 for one variant but < 2 for the other were classified as specific. b, Heatmap of competitive SPR for various antibody groups. The definition of the competition score is described in the Methods section. c, Schematic of the molecular mechanism by which pre-existing IGHV3-53/66-encoded A1 antibodies cause strong immune imprinting. d, Schematic of the antibody passive transfer experiment. Timing of mRNA vaccinations, antibody injection, blood collection, and FACS analysis are indicated. Mice were divided into experimental groups (receiving 400 µg BD55-1205 hlgG1, 200 µg BD55-1205 hlgG1, or 200 µg BD55-1205 mlgG1) and control groups (receiving 200 µg BD57-2665 mlgG1 or PBS). The number of mice per group is indicated at the endpoint. e, DMS escape map logoplots for BD55-1205 and BD57-2665 and their projection onto the SARS-CoV-2 Wuhan RBD (PDB: 6m0j). f, Scatter plots showing the proportion of cross-reactive memory B cells in draining lymph nodes after one (left) or two (right) BA.5 boosts. g, Scatter plots showing the proportion of cross-reactive germinal center B cells in draining lymph nodes after one BA.5 boost. h, Serum IgG midpoint titre against BA.5 RBD before and after Wuhan RBD depletion. Statistical significance of the fold-reduction in titres was assessed between groups. Dashed lines indicate the limit of detection (midpoint titre = 100). Two-tailed Wilcoxon rank-sum tests were used in f-h.

274 at various doses and formats (human or mouse IgG1) one day prior to BA.5 boosting (Fig. 5d-5e).
275 Controls received either PBS or a non-neutralizing antibody (BD57-2665, a representative F1
276 antibody targeting the cryptic sites of RBD, Fig. 5e). Flow cytometry analysis of lymph nodes
277 showed that mice receiving 400 µg or 200 µg BD55-1205 hIgG1 and 200 µg BD55-1205 mIgG1
278 developed pronounced imprinting, evidenced by significantly elevated frequencies of cross-reactive
279 memory B cells at both post-boost time points compared with PBS controls (Fig. 5f). After the first
280 BA.5 boost, GC B cells in BD55-1205–treated mice also showed markedly higher cross-reactivity,
281 demonstrating that early maturation and clonal expansion within the GC was dominated by recalled,
282 imprint-driven B cells (Fig. 5g). In contrast, BD57-2665 mIgG1–treated mice showed no significant
283 change in cross-reactive memory B cell or GC B cell frequencies, indicating that non-neutralizing
284 antibody blockade does not induce imprinting, ruling out the possibility that the transferred antibody
285 simply depleted the vaccine antigen and prevented a successful BA.5 immunization (Fig. 5f-5g).
286 Correspondingly, Wuhan-RBD depletion of serum from BD55-1205–treated mice produced a more
287 severe drop in BA.5 IgG titres, whereas BD57-2665 mIgG1 and PBS groups showed minimal titre
288 reduction (Fig. 5h). Notably, the mIgG1 format induced a significantly stronger imprinting
289 phenotype than hIgG1, which is likely attributable to the species-matched Fc region (Fig. 5f-5h).
290 Pharmacokinetic analysis confirmed that the passively transferred antibodies had decayed to near-
291 undetectable levels by the time of analysis, thus eliminating their potential interference with ELISA
292 measurements (Extended Data Fig. 8a-8b). Importantly, we demonstrated that the suppressive effect
293 of BD55-1205 on the BA.5-specific response was dose-dependent, with doses as low as 12.5 µg
294 being sufficient to achieve inhibition (Extended Data Fig. 8c-8d). Together, these results confirm
295 that IGHV3-53/66-encoded A1 neutralizing antibodies can suppress the emergence of
296 Omicron-specific B cell and antibody responses to induce severe imprinting *in vivo*.

297 This explains why immune imprinting is recapitulated in V(D)J-humanized mice but not in wild-
298 type mice—only the former harbor this human germline gene required to produce such imprinting-
299 prone antibodies. Similarly, consistent with our observation in two human cohorts (Fig. 1f), in
300 mRNA-vaccinated individuals, the potent Wuhan priming response by mRNA vaccination (elicited
301 by monovalent Wuhan vaccines and, in certain populations, bivalent Wuhan/BA.1 or Wuhan/BA.5
302 vaccines) could induce a larger pool of IGHV3-53/66-encoded A1 antibodies, thereby establishing

303 pronounced imprinting. In contrast, recipients of inactivated vaccines typically experience weaker
304 priming responses and, following stringent containment policies during 2021-2022, undergo
305 substantial waning of Wuhan antibodies. This attenuated pre-existing immunity, potentially leading
306 to lower IGHV3-53/66 antibody abundance, fails to fully suppress subsequent Omicron-specific
307 responses, resulting in more flexible and adaptive humoral evolution.

308

309 **IGHV3-53 knock-in mouse model**

310 Since wild-type mice could not recapitulate human SARS-CoV-2 immune imprinting observed in
311 mRNA vaccine recipients, evaluating SARS-CoV-2 vaccine updates and broad-spectrum vaccine
312 design in mice is highly problematic. Although V(D)J-humanized mice could capture human
313 imprinting phenotypes, its significant cost creates a pressing need for a more accessible and cost-
314 effective model for vaccine evaluation. Building on our finding that the human IGHV3-53/66
315 germline is the primary driver of immune imprinting, we engineered a knock-in mouse model by
316 replacing the murine *Ighv3-1* gene with human IGHV3-53 ([Supplementary Information Fig. 4b](#)).
317 This generated both heterozygous (IGHV3-53^{+/-}) and homozygous (IGHV3-53^{+/+}) mice. High-
318 throughput Genome-wide Translocation Sequencing (HTGTS) of the naïve B cell repertoire
319 confirmed the successful knock-in, revealing IGHV3-53 usage at 0.5% in heterozygous and 1.5%
320 in homozygous mice, with a corresponding ablation of *Ighv3-1* usage (0.1% and 0.0%, respectively,
321 [Fig. 6a](#)).

322 To test the model, we immunized wild-type, heterozygous, and homozygous mice using the same
323 regimen of three Wuhan primes followed by two BA.5 boosts ([Fig. 6b](#)). Subsequent flow cytometry
324 analysis and depletion assays confirmed that both IGHV3-53^{+/-} and IGHV3-53^{+/+} mice faithfully
325 recapitulated the strong immune imprinting phenotype ([Fig. 6c-6d](#)). The serum neutralization
326 profiles of IGHV3-53^{+/-} and IGHV3-53^{+/+} mice also showed a trend remarkably similar to that of
327 the V(D)J-humanized mice ([Fig. 6e and Extended Data Fig. 9a](#)). These results demonstrate that both
328 heterozygous and homozygous IGHV3-53 knock-in mice faithfully recapitulate the strong immune
329 imprinting phenotype.

330 We subsequently utilized this model to simulate the real-world SARS-CoV-2 exposure history

Figure 6

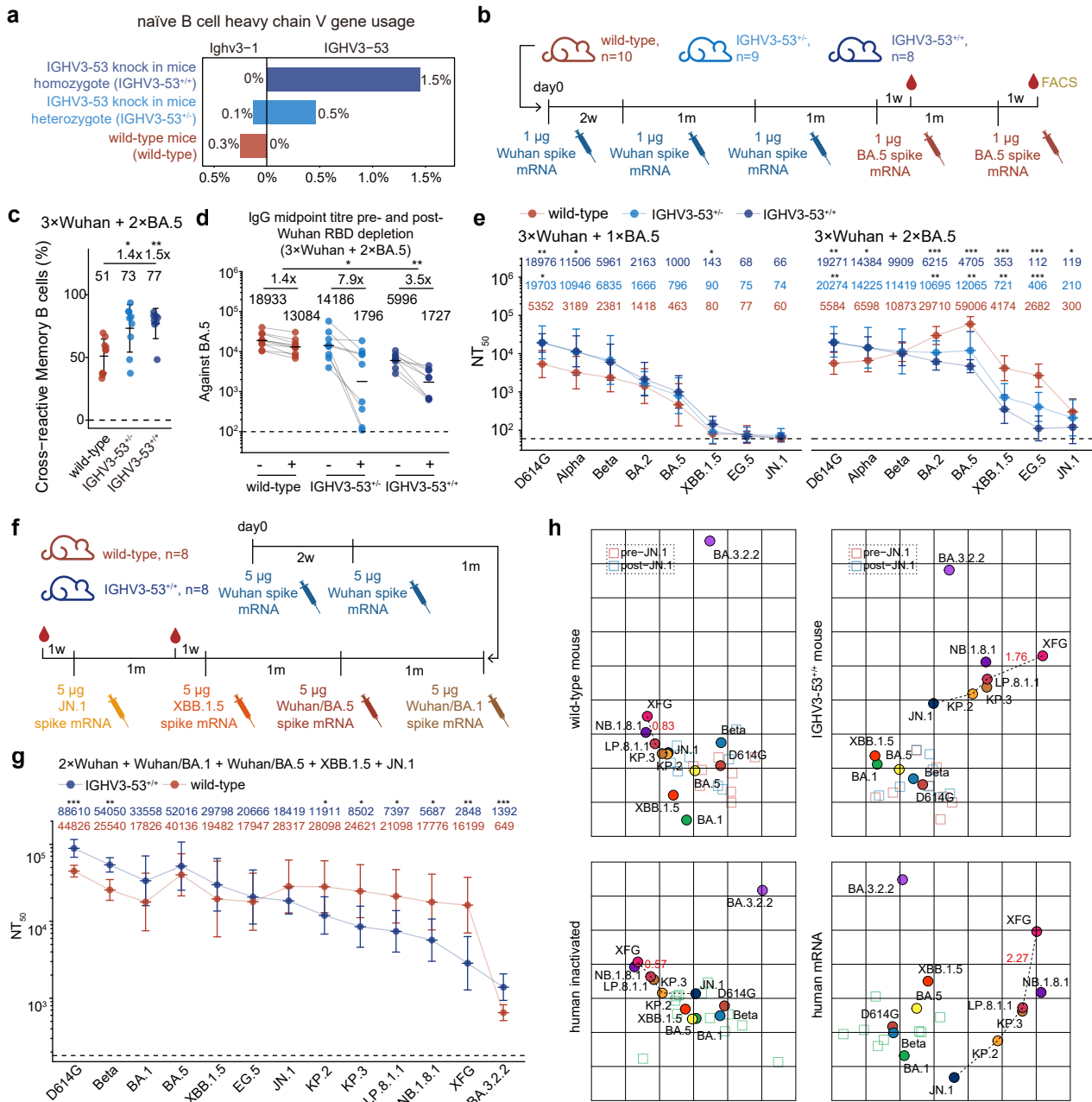


Figure 6 | IGHV3-53 knock-in mice faithfully reflect SARS-CoV-2 antibody map in human.

a. Usage percentage of IGHV3-53 and Ighv3-1 in naïve B cells from HTGTS sequencing of IGHV3-53^{+/+} (balb/c), IGHV3-53^{+/-} (balb/c^{*} C57B6/J), and wild-type (C57B6/J) mice. b. Schematic of the immunization regimen and time points for blood collection and FACS analysis of the three mouse models involved in this study. The number of mice is indicated above the timeline. c. Scatter plots showing the proportion of cross-reactive memory B cells in draining lymph nodes of the three mouse models after two BA.5 boosts. d. Serum IgG midpoint titre of the three mouse strains after two BA.5 boosts against BA.5 RBD before and after Wuhan RBD depletion. Statistical significance of the fold-reduction in titres was assessed between groups. Dashed lines indicate the limit of detection (midpoint titre = 100). e. Serum neutralization titres (NT₅₀) of the three mouse strains after one (left) or two (right) BA.5 boosts against a panel of SARS-CoV-2 variant pseudoviruses. Geometric mean titres (GMTs) are shown on the top. Dashed lines indicate the limit of detection (NT₅₀ = 60). f. Schematic of the immunization regimen simulating real-world SARS-CoV-2 exposure history. g. Serum neutralization titres (NT₅₀) of IGHV3-53^{+/-} and wild-type mice against a panel of SARS-CoV-2 variant pseudoviruses. Geometric mean titres (GMTs) are shown on the top. Dashed lines indicate the limit of detection (NT₅₀ = 180). h. Antigenic cartography was performed using mouse (top) and human (bottom) serum neutralization data. Each square indicates a serum sample, and each circle indicates a SARS-CoV-2 variant. Two-tailed Wilcoxon rank-sum tests were used in c-e and g.

331 characteristic of mRNA-vaccinated populations (Fig. 6f). Specifically, mice received a two-dose
332 Wuhan priming series, mimicking the standard primary course. This was followed by sequential
333 boosters with bivalent Wuhan/BA.1 and Wuhan/BA.5 vaccines, a monovalent XBB.1.5 vaccine,
334 and a monovalent JN.1 vaccine, corresponding to the recommended mRNA booster updates during
335 the Omicron era. These regimens effectively reconstruct the antigenic trajectory of SARS-CoV-2
336 evolution encountered by humans. Compared to wild-type controls, IGHV3-53^{+/+} mice recapitulated
337 a more pronounced immune imprinting phenotype following the six-dose regimen. Specifically,
338 while retaining potent neutralization against D614G and early Omicron variants (antecedent to JN.1,
339 Fig. 6g), IGHV3-53^{+/+} mice exhibited a compromised breadth of neutralization against the newly
340 emerged JN.1 sublineages. Specifically, titres against KP.2, KP.3, LP.8.1.1, NB.1.8.1, and XFG were
341 significantly suppressed compared to those in wild-type mice, indicating an inhibition of *de novo*
342 responses to the newly emerged Omicron-specific epitopes in these variants. (Fig. 6g). Notably,
343 IGHV3-53^{+/+} mice showed higher neutralization titres against BA.3.2.2 than wild-type mice (Fig.
344 6g), mirroring the specific serological feature observed in the human mRNA-vaccinated cohort (Fig.
345 1e). Similar trends were observed after five doses (Extended Data Fig. 10a). Furthermore,
346 comparing neutralization profiles pre- and post-JN.1 boost revealed a strong back-boosting effect
347 in IGHV3-53^{+/+} mice, where JN.1 immunization significantly elevated titres against antecedent
348 strains (pre-JN.1). In contrast, wild-type mice displayed no such effect and even exhibited a
349 significant decline in D614G titres (Extended Data Fig. 10b).

350 Consequently, the two mouse models exhibited distinct susceptibility to viral escape. Following
351 XBB.1.5 immunization, neutralization against EG.5 was significantly reduced compared to
352 XBB.1.5 in IGHV3-53^{+/+} mice, a reduction not seen in wild-type mice (Extended Data Fig. 10c).
353 Similarly, after the JN.1 boost, IGHV3-53^{+/+} mice showed significant susceptibility to escape by
354 KP.2 and KP.3 relative to JN.1, whereas wild-type mice did not. Consistently, the fold-reduction in
355 titres against XFG relative to NB.1.8.1 was greater in IGHV3-53^{+/+} mice than in wild-type mice
356 (Extended Data Fig. 10c). This result faithfully recapitulates the serological divergence observed
357 between the human mRNA-vaccinated and inactivated-only cohorts (Fig. 1e), and matches the
358 variant escaping profiles of V3-53/66 Class 1 NAbs. By leveraging the genetic precision of the
359 IGHV3-53 knock-in model to eliminate confounding immune histories, we definitively confirm that

360 the imprinted, V3-53/66-dominated response inherently renders mRNA recipients more susceptible
361 to immune evasion by such emerging variants.

362 To visualize how IGHV3-53^{+/+} mice could help with SARS-CoV-2 vaccine update evaluation, we
363 constructed antigenic cartography using serum neutralization data from both mouse models and
364 human cohorts (Fig. 6h). The resulting maps revealed striking topological differences. Wild-type
365 mice exhibited a 'condensed' antigenic landscape similar to the inactivated-only cohort,
366 characterized by short antigenic distances between all JN.1 sublineages. In contrast, the antigenic
367 map of IGHV3-53^{+/+} mice closely mirrors that of mRNA-vaccinated cohort, with both displaying
368 substantial antigenic distances between JN.1, KP.2, KP.3/LP.8.1.1, and XFG, supporting vaccine
369 antigen updates. Crucially, only the IGHV3-53^{+/+} model faithfully reproduces the substantial
370 antigenic distance between XFG and LP.8.1.1 characteristic of the mRNA-vaccinated cohort. These
371 findings further implicate the IGHV3-53 knock-in mice could faithfully recapitulates human SARS-
372 CoV-2 immune imprinting, and can serve as a superior model for preclinical SARS-CoV-2 vaccine
373 evaluation.

374

375 **Discussion**

376 Overall, our study establishes that the abundance of pre-existing IGHV3-53/66-encoded Class 1
377 antibodies is the primary determinant of SARS-CoV-2 immune imprinting severity. Specifically,
378 three converging factors—the inherent potent immunogenicity of mRNA platforms in human ⁴⁵, the
379 widespread administration of bivalent mRNA boosters containing Wuhan components in mRNA-
380 vaccinated populations, and the substantial antibody waning in inactivated vaccine recipients due to
381 strict containment policies (e.g., zero-COVID in China) ⁴⁶⁻⁴⁸—sufficiently infer that mRNA
382 vaccinees harbored a significantly higher abundance of IGHV3-53/66-encoded Class 1 antibodies
383 prior to their first Omicron exposure. Consequently, this mRNA-vaccinated population exhibits a
384 more robust humoral imprinting phenotype. As these distinct humoral immune landscapes became
385 established, a parallel divergence in viral evolution emerged, characterized by the regional
386 predominance of XFG and NB.1.8.1. This co-evolution highlights the necessity of incorporating
387 regional immunological differences into vaccine update strategies.

388 We acknowledge that the sample size of our human cohorts was relatively small, and intrinsic
389 individual heterogeneity could not be fully controlled. However, the findings align well with
390 previous studies and were mechanistically corroborated by our animal models. This consistency
391 confirms the validity of our head-to-head comparisons and the real-world impact of immune
392 imprinting on regional epidemiology. Additionally, we acknowledge the individual heterogeneity
393 within our humanized mouse model, where a part of them exhibited weaker immune imprinting. We
394 hypothesize that the isolated Omicron-specific A2 antibodies likely derived from these mice.
395 Although the pooling of samples during B cell sorting prevents us from retrospectively tracing
396 specific antibodies to individual animals, the existence of these outlier responses does not
397 undermine our core conclusions that humanized mice collectively develop a significantly stronger
398 imprinting phenotype in both serum and memory B cell compartments. These "outlier" mice likely
399 resemble inactivated vaccine recipients, where the abrupt exposure to BA.5 resulted in extensive
400 escape of pre-existing A1 antibodies, leaving insufficient cross-reactive binding to effectively mask
401 Omicron-specific epitopes. In contrast, sequential exposure to BA.1/BA.2 in mRNA vaccinees
402 involved a gradual antigenic shift, allowing A1 antibodies to mature and expand without facing the
403 drastic escape seen with BA.5. This preserved a sufficient cross-reactive pool to effectively mask
404 the *de novo* response upon the subsequent BA.5 exposure.

405 Importantly, we developed an accessible and robust IGHV3-53 knock-in mouse model that
406 overcomes the limitations of wild-type mice, which fail to recapitulate the SARS-CoV-2 imprinting
407 phenotype. By simulating real-world SARS-CoV-2 exposure histories in this model, we successfully
408 mapped the humoral response landscape of mRNA human vaccinees in mice. Moving forward, this
409 model should be leveraged to conduct parallel evaluations of boosting regimens derived from
410 diverse, newly emerging variants. Such comparative studies will provide the essential data support
411 required to guide the further updating and optimization of SARS-CoV-2 vaccines. Furthermore, as
412 a platform that explicitly exposes the 'imprinted barrier' of mRNA recipients, it would enable the
413 future research of vaccine candidates capable of overcoming such entrenched imprinting.

414

415 **Data and code availability**

416 Information of individuals providing blood samples and isolated mAbs involved in this study have
417 been included in the Supplementary Tables. All data and materials presented in this manuscript are
418 available from the lead contact upon a reasonable request under a completed Material Transfer
419 Agreement. Further information and requests for resources and reagents should be directed to and
420 will be fulfilled by the lead contact, yunlongcao@pku.edu.cn (Y.C.).

421 **Acknowledgments**

422 We thank all volunteers who provided blood samples. This project is financially supported by the
423 Ministry of Science and Technology of China (2022ZD0115002, Y.C.) and Changping Laboratory
424 (2025D-04-01 to Y.C.).

425 **Author contributions**

426 Y.C. designed and supervised the study. X.N., F.J. and Y.C. wrote the manuscript with input from
427 all authors. X.N., W.S., R.A. and Y.W. performed B cell sorting, single-cell V(D)J sequencing
428 experiments and data analysis. X.N., Y.L., K.L., S.L., R.K., X.C., R.A., and Y.W. performed FACS
429 analysis. H.S. and F.J. obtained and analyzed the DMS data. J.W. and F.S. performed antibody
430 expression. W.W. constructed mRNA vaccines and conducted mouse immunization. Y.Y.
431 constructed the pseudotyped virus. L.Y. performed the pseudovirus neutralization assays, ELISAs
432 and SPR experiments. Y.H., S.L., X.N. and Y.L. performed the HTGTS-Rep-seq and data analysis.
433 B.Z., T.Z., J.H., and X.T. recruited the patients and collected the blood samples.

434 **Declaration of interests**

435 Provisional patents related to the antibodies mentioned in this paper have been filed. Y.C. is a co-
436 founder of Singlomics Biopharmaceuticals. Other authors declare no competing interests.

437

438 **References**

- 439 1. Uraki, R., Korber, B., Diamond, M. S. & Kawaoka, Y. SARS-CoV-2 variants: biology,
440 pathogenicity, immunity and control. *Nat. Rev. Microbiol.* **24**, 8–28 (2026).
- 441 2. Liang, C.-Y. *et al.* Imprinting of serum neutralizing antibodies by Wuhan-1 mRNA
442 vaccines. *Nature* 1–3 (2024) doi:10.1038/s41586-024-07539-1.
- 443 3. Tortorici, M. A. *et al.* Persistent immune imprinting occurs after vaccination with the

- 444 COVID-19 XBB.1.5 mRNA booster in humans. *Immunity* **57**, 904-911.e4 (2024).
- 445 4. Wang, Q. *et al.* Deep immunological imprinting due to the ancestral spike in the current
446 bivalent COVID-19 vaccine. *Cell Rep. Med.* **4**, (2023).
- 447 5. Reynolds, C. J. *et al.* Immune boosting by B.1.1.529 (Omicron) depends on previous
448 SARS-CoV-2 exposure. *Science* **377**, eabq1841 (2022).
- 449 6. Chemaitelly, H. *et al.* Long-term COVID-19 booster effectiveness by infection history and
450 clinical vulnerability and immune imprinting: a retrospective population-based cohort study.
451 *Lancet Infect. Dis.* **23**, 816–827 (2023).
- 452 7. Wang, Z. *et al.* Memory B cell responses to Omicron subvariants after SARS-CoV-2
453 mRNA breakthrough infection in humans. *J. Exp. Med.* **219**, e20221006 (2022).
- 454 8. Wang, Q. *et al.* XBB.1.5 monovalent mRNA vaccine booster elicits robust neutralizing
455 antibodies against XBB subvariants and JN.1. *Cell Host Microbe* **32**, 315-321.e3 (2024).
- 456 9. Johnston, T. S. *et al.* Immunological imprinting shapes the specificity of human antibody
457 responses against SARS-CoV-2 variants. *Immunity* **57**, 912-925.e4 (2024).
- 458 10. Addetia, A. *et al.* Neutralization, effector function and immune imprinting of Omicron
459 variants. *Nature* **621**, 592–601 (2023).
- 460 11. Yisimayi, A. *et al.* Prolonged Omicron-specific B cell maturation alleviates immune
461 imprinting induced by SARS-CoV-2 inactivated vaccine. *Emerg. Microbes Infect.* **13**, 2412623
462 (2024).
- 463 12. Chen, Y. *et al.* SARS-CoV-2 Omicron infection augments the magnitude and durability
464 of systemic and mucosal immunity in triple-dose CoronaVac recipients. *mBio* **15**, e02407-23
465 (2024).
- 466 13. Yisimayi, A. *et al.* Repeated Omicron exposures override ancestral SARS-CoV-2 immune
467 imprinting. *Nature* **625**, 148–156 (2024).
- 468 14. Yang, X. *et al.* Immune imprinting toward SARS-CoV-2 XBB: implications for vaccine
469 strategy and variant risk assessment. *Signal Transduct. Target. Ther.* **10**, 372 (2025).
- 470 15. Korber, B., Fischer, W. & Theiler, J. Real-time monitoring of SARS-CoV-2 evolution during
471 the COVID-19 pandemic. *Cell Host Microbe* **33**, 1802–1806 (2025).
- 472 16. Mellis, I. A. *et al.* Antibody evasion and receptor binding of SARS-CoV-2 LP.8.1.1,
473 NB.1.8.1, XFG, and related subvariants. *Cell Rep.* **44**, 116440 (2025).
- 474 17. Guo, C. *et al.* Antigenic and virological characteristics of SARS-CoV-2 variants BA.3.2,
475 XFG, and NB.1.8.1. *Lancet Infect. Dis.* **25**, e374–e377 (2025).
- 476 18. Uriu, K. *et al.* Virological characteristics of the SARS-CoV-2 NB.1.8.1 variant. *Lancet Infect.*
477 *Dis.* **25**, e443 (2025).
- 478 19. Cao, G., Xu, C., Wang, L., Chai, K. & Wu, B. Global Surveillance and Biological
479 Characterization of the SARS-CoV-2 NB.1.8.1 Variant: An Emerging VUM Lineage Under
480 Scrutiny. *Viruses* **17**, 1457 (2025).
- 481 20. Kaku, Y. *et al.* Humoral immunity induced by LP.8.1 monovalent vaccines against a broad
482 range of SARS-CoV-2 variants including XEC, NB.1.8.1, XFG, and BA.3.2. 2025.11.18.689152
483 Preprint at <https://doi.org/10.1101/2025.11.18.689152> (2025).
- 484 21. Mellis, I. A. *et al.* Antibody evasion and receptor binding of SARS-CoV-2 LP.8.1.1,
485 NB.1.8.1, XFG, and related subvariants. *Cell Rep.* **44**, (2025).
- 486 22. Wang, Q. *et al.* Antibody evasiveness of SARS-CoV-2 subvariants KP.3.1.1 and XEC. *Cell*
487 *Rep.* **44**, (2025).

- 488 23. Li, P. *et al.* Neutralization and spike stability of JN.1-derived LB.1, KP.2.3, KP.3, and
489 KP.3.1.1 subvariants. *mBio* **16**, e00464–25 (2025).
- 490 24. Li, P. *et al.* Neutralization escape, infectivity, and membrane fusion of JN.1-derived SARS-
491 CoV-2 SLip, FLiRT, and KP.2 variants. *Cell Rep.* **43**, (2024).
- 492 25. Wang, Q. *et al.* Robust SARS-CoV-2-neutralizing antibodies sustained through 6 months
493 post XBB.1.5 mRNA vaccine booster. *Cell Rep. Med.* **5**, (2024).
- 494 26. Jian, F. *et al.* Evolving antibody response to SARS-CoV-2 antigenic shift from XBB to JN.1.
495 *Nature* **637**, 921–929 (2025).
- 496 27. Liu, J. *et al.* Enhanced immune evasion of SARS-CoV-2 variants KP.3.1.1 and XEC through
497 N-terminal domain mutations. *Lancet Infect. Dis.* **25**, e6–e7 (2025).
- 498 28. Liu, J. *et al.* Virological and antigenic characteristics of SARS-CoV-2 variants LF.7.2.1, NP.1,
499 and LP.8.1. *Lancet Infect. Dis.* **25**, e128–e130 (2025).
- 500 29. Yang, S. *et al.* Fast evolution of SARS-CoV-2 BA.2.86 to JN.1 under heavy immune
501 pressure. *Lancet Infect. Dis.* **24**, e70–e72 (2024).
- 502 30. Tiller, T. *et al.* Efficient generation of monoclonal antibodies from single human B cells by
503 single cell RT-PCR and expression vector cloning. *J. Immunol. Methods* **329**, 112–124 (2008).
- 504 31. Yuan, M. *et al.* Structural basis of a shared antibody response to SARS-CoV-2. *Science*
505 <https://doi.org/10.1126/science.abd2321> (2020) doi:10.1126/science.abd2321.
- 506 32. Wang, Y. *et al.* A large-scale systematic survey reveals recurring molecular features of
507 public antibody responses to SARS-CoV-2. *Immunity* **55**, 1105–1117.e4 (2022).
- 508 33. Li L. *et al.* Breakthrough infection elicits hypermutated IGHV3-53/3-66 public antibodies
509 with broad and potent neutralizing activity against SARS-CoV-2 variants including the
510 emerging EG.5 lineages. *PLOS Pathog.* **19**, e1011856 (2023).
- 511 34. Vanshylla, K. *et al.* Discovery of ultrapotent broadly neutralizing antibodies from SARS-
512 CoV-2 elite neutralizers. *Cell Host Microbe* **30**, 69–82.e10 (2022).
- 513 35. Yan, Q. *et al.* Germline IGHV3-53-encoded RBD-targeting neutralizing antibodies are
514 commonly present in the antibody repertoires of COVID-19 patients. *Emerg. Microbes Infect.*
515 **10**, 1097–1111 (2021).
- 516 36. Zhang, Q. *et al.* Potent and protective IGHV3-53/3-66 public antibodies and their shared
517 escape mutant on the spike of SARS-CoV-2. *Nat. Commun.* **12**, 4210 (2021).
- 518 37. Nutalai, R. *et al.* Potent cross-reactive antibodies following Omicron breakthrough in
519 vaccinees. *Cell* **185**, 2116–2131.e18 (2022).
- 520 38. Tan, T. J. C. *et al.* Sequence signatures of two public antibody clonotypes that bind SARS-
521 CoV-2 receptor binding domain. *Nat. Commun.* **12**, 3815 (2021).
- 522 39. Cao, Y. *et al.* Omicron escapes the majority of existing SARS-CoV-2 neutralizing
523 antibodies. *Nature* **602**, 657–663 (2022).
- 524 40. Cao, Y. *et al.* Characterization of the enhanced infectivity and antibody evasion of
525 Omicron BA.2.75. *Cell Host Microbe* **30**, 1527–1539.e5 (2022).
- 526 41. Cao, Y. *et al.* Rational identification of potent and broad sarbecovirus-neutralizing
527 antibody cocktails from SARS convalescents. *Cell Rep.* **41**, 111845 (2022).
- 528 42. Cao, Y. *et al.* BA.2.12.1, BA.4 and BA.5 escape antibodies elicited by Omicron infection.
529 *Nature* **608**, 593–602 (2022).
- 530 43. Cao, Y. *et al.* Imprinted SARS-CoV-2 humoral immunity induces convergent Omicron
531 RBD evolution. *Nature* **614**, 521–529 (2023).

- 532 44. Jian, F. *et al.* Viral evolution prediction identifies broadly neutralizing antibodies to
533 existing and prospective SARS-CoV-2 variants. *Nat. Microbiol.* 1–15 (2025)
534 doi:10.1038/s41564-025-02030-7.
- 535 45. Lim, W. W., Mak, L., Leung, G. M., Cowling, B. J. & Peiris, M. Comparative immunogenicity
536 of mRNA and inactivated vaccines against COVID-19. *Lancet Microbe* **2**, e423 (2021).
- 537 46. Xu, W., Wu, J. & Cao, L. COVID-19 pandemic in China: Context, experience and lessons.
538 *Health Policy Technol.* **9**, 639–648 (2020).
- 539 47. Bo, W. *et al.* The current COVID-19 pandemic in China: An overview and corona data
540 analysis. *Alex. Eng. J.* **61**, 1369–1381 (2022).
- 541 48. Gauffin K., Östergren O. & Cederström A. The global response to the pandemic: An
542 empirical cluster analysis of policies targeting COVID-19. *PLOS ONE* **20**, e0322692 (2025).
- 543 49. Yanez Arteta, M. *et al.* Successful reprogramming of cellular protein production through
544 mRNA delivered by functionalized lipid nanoparticles. *Proc. Natl. Acad. Sci.* **115**, E3351–E3360
545 (2018).
- 546 50. Li, H. *et al.* Establishment of replication-competent vesicular stomatitis virus-based
547 recombinant viruses suitable for SARS-CoV-2 entry and neutralization assays. *Emerg.*
548 *Microbes Infect.* **9**, 2269–2277 (2020).
- 549 51. Ye, J., Ma, N., Madden, T. L. & Ostell, J. M. IgBLAST: an immunoglobulin variable domain
550 sequence analysis tool. *Nucleic Acids Res.* **41**, W34–W40 (2013).
- 551 52. Gupta, N. T. *et al.* Change-O: a toolkit for analyzing large-scale B cell immunoglobulin
552 repertoire sequencing data. *Bioinformatics* **31**, 3356–3358 (2015).
- 553 53. Lin, S. G. *et al.* Highly sensitive and unbiased approach for elucidating antibody
554 repertoires. *Proc. Natl. Acad. Sci.* **113**, 7846–7851 (2016).
- 555 54. Traag, V. A., Waltman, L. & van Eck, N. J. From Louvain to Leiden: guaranteeing well-
556 connected communities. *Sci. Rep.* **9**, 5233 (2019).

557

558 **Methods**

559 **Human serum and PBMC isolation**

560 Blood samples were obtained from convalescent individuals who had received various vaccine
561 platforms (detailed in Supplementary Table 1). The research protocol and the collection of human
562 blood samples were approved by the Institutional Review Board (IRB) of Shenzhen Institute of
563 Advanced Science, Chinese Academy of Science (Ethics committee archiving no. SIAT-IRB-
564 230715-H0667) and Beijing Ditan Hospital, Capital Medical University (Ethics committee
565 archiving no. DTEC-KY2024-112-01). All participants provided their agreement for the collection,
566 storage and use of their blood samples strictly for research purposes and the subsequent publication
567 of related data.

568 To isolate serum and PBMCs, whole blood was diluted 1:1 with PBS (Invitrogen, C10010500BT)

569 containing 2% (v/v) fetal bovine serum (FBS; Hyclone, SH30406.05) and separated by density
570 gradient centrifugation using Ficoll (Cytiva, 17-1440-03). The upper serum layer was collected,
571 aliquoted, and stored at or below -20°C. Before use in assays, serum samples were heat-inactivated
572 and assessed for neutralizing titres against SARS-CoV-2 variant spike-pseudotyped vesicular
573 stomatitis virus (VSV).

574 The PBMC layer was harvested from the interface and processed further. Following red blood cell
575 lysis (Invitrogen eBioscience 1X RBC Lysis Buffer, 00-4333-57) and washing, PBMCs were either
576 used immediately or cryopreserved in FBS with 10% (v/v) DMSO (Solarbio, D8371) for storage in
577 liquid nitrogen. All PBMC samples were transported on dry ice. For B cell isolation, cryopreserved
578 PBMCs were thawed in PBS supplemented with 5% (v/v) FBS. B cells were subsequently enriched
579 by immunomagnetic positive selection using the EasySep™ Human CD19 Positive Selection Kit II
580 (STEMCELL, 17854) following the manufacturer's protocol. The resulting purified B cells were
581 resuspended in PBS with 2% (v/v) FBS, and cell counts and viability were determined using 0.4%
582 (w/v) trypan blue staining (Invitrogen, T10282) on a Countess Automated Cell Counter (Invitrogen).

583 **Mice**

584 All animal experiments were conducted under protocols approved by the Animal Welfare Ethics
585 Committee of HFK Biologics (Approval No. HFK-AP-20250313). The humanized mouse model
586 (NeoMab-IgG), provided by NeoMab Biotechnology Co., Ltd., was created by in situ replacing the
587 mouse heavy chain variable region genes and kappa light chain variable region genes with human
588 genes in BALB/c mouse background. The mouse constant region genes were retained, making sure
589 the Fc of the immunoglobulins can interact with the Fc receptors expressed on other immune cells
590 normally, supporting standard immune system development and response. The IGHV3-53^{+/+} or
591 IGHV3-53^{+/-} mice were generated by Cyagen Biosciences (Suzhou, China). To generate these mice,
592 the targeting construct replaced the sequence from ATG start codon to exon 3 of mouse *Ighv3-1* by
593 the sequence from ATG start codon to exon 2 of the human IGHV3-53, including the introns. The
594 Cas9 protein, construct and guide RNAs (gRNA-A1: 5'-TGAGAGTGCTGATTCTTTTGTGG-3',
595 gRNA-A2: 5'-TGCAGTGCTGCTCTGCAAGGAGG-3' and gRNA-B1: 5'-
596 TGGCTGTTACAGCCTTTCCTGG-3', gRNA-B2: 5'-TGGTGCAGTGCTGCTCTGCAAGG-3')
597 were microinjected into zygotes from BALB/cAnCya wild-type mice. The embryos were

598 transferred to recipient female mice to obtain F0 mice. The genotype of IGHV3-53^{+/+} or IGHV3-
599 53^{+/-} mice was confirmed by PCR using two pairs of primers (F4: 5'-
600 CACCATCTCCAGAGACAATTCCAAG-3', R3: 5'-GTTCTGGATACCAATGTGCCTTCAG-3'
601 and F3: 5'-TGCAGTCAGTAGCCACCTCGCCAAT-3', R4: 5'-
602 CATCAGACAGGATACCTTCAGAGAAG-3') and sequencing. Mice of all strains (6–8 weeks old)
603 were housed under specific-pathogen-free (SPF) conditions, maintained at 22 ± 2°C with 50–60%
604 humidity on a 12-hour light/dark cycle. All animals had *ad libitum* access to standard chow and
605 sterile water. Due to the limited availability of the IGHV3-53 knock-in mice, the sample size and
606 sex distribution varied slightly across the experimental groups shown in Figure 6. Female mice were
607 used for the VDJ-humanized and wild-type BALB/c models, while both sexes were used for the
608 IGHV3-53 knock-in models. Sex distribution was 4 males and 4 females for IGHV3-53^{+/+} mice, 3
609 males and 6 females for IGHV3-53^{+/-} mice in figure 6b, and 4 males and 4 females for IGHV3-53^{+/+}
610 mice in figure 6f.

611 **mRNA-LNP Synthesis and Formulation**

612 A PSP73 plasmid bearing the antigen insert followed by a 120-nt poly(T) tract was linearized with
613 the appropriate restriction enzyme. This DNA served as a template for *in vitro* transcription process
614 to generate RNA that encoded the SARS-CoV-2 Wuhan, BA.1, BA.5, XBB.1.5 and JN.1 S6P (F817P,
615 A892P, A899P, A942P, K986P, V987P, R683A and R685A) protein. Linearized DNA template (1
616 µg) was transcribed for 2 hours at 37°C using the EasyCap T7 Co-transcription Kit with CAG
617 Trimer (Vazyme, DD4203). Following transcription, the DNA template was digested by incubation
618 with 1 U of RNase-free DNase I for 15 minutes at 37°C. The resulting mRNA was purified with
619 VAHTS RNA Clean Beads (Vazyme, N412-03). The concentration and purity of the purified mRNA
620 were determined by UV spectrophotometry (absorbance at 260 nm and A260/A280), and its
621 integrity was verified by agarose gel electrophoresis.

622 The mRNA was encapsulated in a functionalized lipid nanoparticle (LNP) as described previously
623 ⁴⁹. The lipid mixture (oil phase) was prepared by dissolving SM-102, DSPC, cholesterol, and DMG-
624 PEG2000 in 100 % ethanol at a molar ratio of 50:10:38.5:1.5 to a total concentration of 9.04 mg/mL.
625 The filter-sterilized (0.22 µm) aqueous phase, consisting of 50 mM sodium citrate buffer (pH 4.0),
626 and the purified mRNA was diluted within it to a concentration of 133 µg/mL. Oil and aqueous

627 phases were then rapidly mixed at a 3:1 volume ratio using a staggered herringbone micromixer,
628 operating at a total flow rate of 12 mL/min to induce LNP self-assembly. The crude LNP suspension
629 underwent buffer exchange and purification via overnight dialysis at 4°C against a solution of 10
630 mM Tris-HCl (pH 7.4) with 8-10% (w/v) sucrose, using 10 kDa MWCO dialysis cassettes. The
631 dialyzed LNPs were subsequently concentrated by centrifugation at 1,500-2,500 × g for 10-15
632 minutes at 4°C using 10 kDa MWCO ultrafiltration units (ULRC0100150P). The final formulation
633 was adjusted to a sucrose concentration of 8.7% (w/v), aliquoted, flash-frozen in liquid nitrogen,
634 and stored at -80°C.

635 The final product was subjected to rigorous quality control. Key attributes including particle size
636 (by dynamic light scattering), RNA encapsulation efficiency (by RiboGreen assay), mRNA integrity
637 (by capillary electrophoresis), osmolality, and endotoxin levels (by LAL assay) were assessed. All
638 manufactured batches were required to meet the following release criteria: a particle diameter of 80-
639 100 nm, ≥90% RNA encapsulation, ≥80% mRNA integrity, and an endotoxin level below 1 EU/mL.

640 **Mouse immunization and passive antibody transfer**

641 For immunization, mice were administered mRNA-LNP vaccines. The specific immunization
642 regimens, including vaccine type, dosage, and timelines, are detailed in the schematics of Figure 2a,
643 5d, 6b, 6f and Extended Data figure 11a and 11c. On the day of administration, LNP-mRNA vials
644 were thawed on ice and diluted in sterile 1× PBS to the appropriate concentration. Each mouse was
645 injected intramuscularly (i.m.) into the quadriceps muscle with 100 µL of the vaccine solution using
646 a 29 G insulin syringe. To prevent leakage of the inoculum, the needle was held in place for 3–5
647 seconds post-injection.

648 For passive antibody transfer, purified mAbs (BD55-1205-mIgG1, BD55-1205-hIgG1, or BD57-
649 2665-mIgG1) with low endotoxin levels (<0.02 EU/mg) were used. The antibodies were diluted in
650 sterile PBS to the desired concentration for injection. Female BALB/c mice (6–8 weeks old)
651 received a 200 µL dose via intraperitoneal (i.p.) injection in the left lower quadrant using a 26 G
652 needle. Mice were monitored for at least 5 minutes following the injection, and any subsequent
653 doses were administered according to the specified experimental schedules.

654 **Pseudovirus preparation and neutralization assay**

655 We generated SARS-CoV-2 variant spike protein pseudovirus as described previously^{13,17,26–28,50}.
656 Plasmids encoding a codon-optimized SARS-CoV-2 Spike (S) protein were constructed by inserting
657 the S gene into the pcDNA3.1 vector. To produce pseudovirus, 293T cells (ATCC, CRL-3216) were
658 transfected with the S protein expressing plasmids with Lipofectamine 3000 (Invitrogen, L3000015)
659 and subsequently infected with G*ΔG-VSV (Kerafast, EH1020-PM). After 24 hours, the
660 supernatant containing the pseudovirus was harvested, filtered through a 0.45 μm filter (Millipore),
661 aliquoted, and stored at -80°C.

662 Neutralization assays were performed using the Huh-7 cell line (JCRB, 0403). Monoclonal
663 antibodies or serum samples were serially diluted in DMEM (Hyclone, SH30243.01) and incubated
664 with the pseudovirus in 96-well plates for 1 hour at 37°C with 5% CO₂. Following incubation, Huh-
665 7 cells were seeded into the wells (2×10⁴ cells per well) and cultured for an additional 24 hours at
666 37°C with 5% CO₂. To assess infection levels, the culture supernatant was removed and left 100 μ
667 l in each well. The Bright-Lite Luciferase Assay Substrate was reconstituted with its corresponding
668 Assay Buffer (Vazyme, DD1209-03-AB), and this mixture was added to the wells. After incubating
669 in the dark for 2 minutes, luminescence was measured using a microplate spectrophotometer
670 (PerkinElmer, HH3400). The NT₅₀ or IC₅₀ values were determined using a three-parameter logistic
671 regression model.

672 **Mouse tissue processing and B cell extraction**

673 Following euthanasia, the spleen, inguinal lymph nodes, and popliteal lymph nodes were harvested
674 and placed in RPMI 1640 culture medium (Invitrogen, C11875500CP) containing 5% (v/v) FBS.
675 Single-cell suspensions were prepared by mechanical disruption using the plunger of a syringe. The
676 popliteal and inguinal lymph nodes from each mouse were pooled, ground, and filtered through a
677 40 μm cell strainer. For the spleen, tissue was processed by the same grinding method and passed
678 through a 70 μm cell strainer, followed by centrifugation and lysis of red blood cells using 1× RBC
679 Lysis Buffer (Invitrogen eBioscience, 00-4333-57). After washing steps and centrifugation, the
680 resulting cell pellets were resuspended in PBS containing 2% (v/v) FBS.

681 Splenic B cells were enriched from the splenic single-cell suspensions via immunomagnetic
682 negative selection with the EasySep™ Mouse Pan-B Cell Isolation Kit (STEMCELL, 19844).

683 Following the manufacturer's protocol, the untouched, purified B cells were collected and washed
684 in PBS with 2% (v/v) FBS. The cell numbers of total lymph node cells and purified splenic B cells
685 were determined using 0.4% (w/v) trypan blue stain (Invitrogen, T10282) and a Countess
686 Automated Cell Counter (Invitrogen).

687 **Flow cytometry analysis and antigen-specific B cell sorting**

688 For the isolation of antigen-specific human B cells, enriched B cell populations from PBMCs were
689 prepared for fluorescence-activated cell sorting (FACS). The staining panel included FITC anti-
690 human CD20 (BioLegend, 302304), Brilliant Violet 605™ anti-human CD27 (BioLegend, 302824),
691 PE/Cyanine7 anti-human IgM (BioLegend, 314532), and PE/Cyanine7 anti-human IgD (BioLegend,
692 348210). Antigen-specific cells were detected using biotinylated JN.1 RBD (Sino Biological,
693 40592-V49H16-B) conjugated with PE-streptavidin (BioLegend, 405204) and APC-streptavidin
694 (BioLegend, 405207), and Wuhan RBD (Sino Biological, 40592-V27H-B) conjugated with BV421-
695 streptavidin (BioLegend, 405225). The viability dye 7-AAD (Invitrogen, 00-6993-50) was used to
696 exclude dead cells. A gating strategy was applied to sort single, viable (7-AAD⁻), class-switched
697 (IgM⁻ and IgD⁻), CD20⁺CD27⁺ memory B cells that were positive for JN.1 RBD.

698 For the characterization of B cell responses in immunized mice, single-cell suspensions from the
699 inguinal and popliteal lymph nodes were stained for flow cytometry analysis. The cells were stained
700 with a panel including PE/Cyanine7 anti-mouse CD38 (BioLegend, 102718), Brilliant Violet 605™
701 anti-mouse/human B220 (BioLegend, 103244), APC/Cyanine7 anti-mouse IgD (BioLegend,
702 405716), Brilliant Violet 711™ anti-mouse IgM (BioLegend, 406539), and FITC anti-mouse/human
703 GL7 (BioLegend, 144603). The antigen probe cocktail consisted of biotinylated BA.5 RBD (Sino
704 Biological, 40592-V49H9-B) conjugated with PE- and APC-streptavidin, and Wuhan RBD
705 conjugated with BV421-streptavidin. Data for lymph node analysis were acquired on a Symphony
706 A5SE cytometer (BD Biosciences).

707 For the isolation of antigen-specific mouse splenic B cells, purified splenic B cells were stained
708 using the identical panel of antibodies and RBD probes as described for the lymph node analysis.
709 MoFlo Astrios EQ Cell Sorter (Beckman Coulter) was used for all sorting experiments, targeting
710 live (7-AAD⁻), B220⁺, CD38⁺, class-switched (IgM⁻ and IgD⁻), non-germinal center (GL7⁻) B cells

711 that bound to the BA.5 RBD.

712 For all procedures, data were collected via Summit 6.0 software (Beckman Coulter). Data from all
713 experiments were uniformly analyzed using FlowJo v10.8 (BD Biosciences).

714 **Single-cell V(D)J sequencing**

715 For the 10X Genomics workflow, sorted antigen-specific B cells, suspended in PBS with 10% (v/v)
716 FBS, were processed with the Chromium Next GEM Single Cell V(D)J Reagent Kits v1.1 (10X
717 Genomics, CG000208). The cell suspension was loaded onto a 10X Chromium Controller to
718 generate Gel Beads-in-Emulsion (GEMs), which facilitate the barcoding of mRNA and subsequent
719 reverse transcription within individual droplets. Following cDNA synthesis, the product was
720 purified using a SPRIselect Reagent Kit (Beckman Coulter, B23318) and pre-amplified. Targeted
721 enrichment of paired V(D)J sequences was then achieved using 10X-specific BCR primers, and the
722 resulting products were used for sequencing library construction. These final libraries were
723 sequenced on an Illumina NovaSeq 6000 platform with a NovaSeq 6000 S4 Reagent Kit v1.5 (300
724 cycles; Illumina, 20028312). The 10X Genomics V(D)J Illumina sequencing data were assembled
725 as B cell receptor contigs and aligned to the B cell V(D)J reference using Cell Ranger (v.6.1.1)
726 pipeline. For human-source IGH and IGK contigs, we use GRCh38 as reference. For mouse-source
727 IGL contigs, we use GRCm38 as reference. Only the productive contigs and B cells with one heavy
728 chain and one light chain were kept to remove doublets. The germline V(D)J genes were identified
729 and annotated using IgBlast (v1.17.1)⁵¹. SHM nucleotides and residues in the antibody variable
730 domain were detected using Change-O toolkit (v.1.2.0)⁵².

731 For the plate-based method, single antigen-specific B cells were sorted directly into the individual
732 wells of 96-well plates, each containing 4 μ L of lysis buffer (0.095% Triton X-100, 2.5 μ M oligo-
733 dT primer: 5'-
734 AAGCAGTGGTATCAACGCAGAGTACTTTTTTTTTTTTTTTTTTTTTTTTTTTTTTTVN-3',
735 2.5 mM dNTPs, 1 U/ μ L RNase Inhibitor). The plates were immediately processed by vortexing,
736 centrifugation, and incubation at 72°C for 3 min to denature RNA secondary structures, followed
737 by rapid chilling on ice. Reverse transcription was performed in each well by adding 5.7 μ L of an
738 RT master mix (final concentrations: 1 \times HiScript III first-strand buffer, 10 U/ μ L HiScript III

739 reverse transcriptase, 2 U/ μ L RNase inhibitor, 5 mM DTT, 1 M betaine, 6 mM MgCl₂, 1 μ M TSO
740 primer: 5'-AAGCAGTGGTATCAACGCAGAGTACATrGrG+G-3'). The RT reaction was
741 incubated at 37°C for 60 minutes, followed by enzyme inactivation at 85°C for 5 seconds. The
742 resulting cDNA served as a template for amplifying full-length immunoglobulin heavy and light
743 chain V(D)J sequences via a two-round nested PCR strategy using Phanta Max Master Mix (Vazyme,
744 P515). The first PCR round employed a multiplex primer pool targeting all VH, V κ , and V λ gene
745 families, along with constant region-specific reverse primers. A second, nested PCR round was then
746 performed with internal primers to enhance specificity and yield. Final amplicons were purified and
747 subsequently analyzed by Sanger sequencing. The germline V(D)J genes were identified and
748 annotated using IgBlast (v1.22.0)⁵¹.

749 **HTGTS-Rep-seq**

750 0.5-4 μ g of genomic DNA from purified splenic B cells was used for generating HTGTS-Rep-seq
751 libraries as previously described⁵³. Four bait primers that target mouse JH1 (5'-
752 TGACATGGGGAGATCTGAGA-3'), JH2 (5'-CCCCAACAAATGCAGTAAAATCT-3'), JH3 (5'-
753 GAGAATCTTGGTCCTGAAGGC-3'), and JH4 (5'-CTGCAATGCTCAGAAAACCTCC-3') were
754 mixed to capture all heavy chain (HC) repertoire in one library. All primers carried a 5' biotin
755 modification (5BiosG). These HTGTS-Rep-seq libraries were sequenced on DNBSEQ-T7. Data
756 were analyzed with the HTGTS-Rep-seq pipeline⁵³.

757 **Monoclonal antibody expression and purification**

758 The sequences for the antibody heavy and light chains were initially codon-optimized for expression
759 in human cells (GenScript). The variable regions (VH and VL) were then separately inserted into
760 corresponding expression vectors (pCMV3-CH, pCMV3-CL or pCMV3-CK). Plasmids of the
761 heavy and light chain constructs were transformed into *Escherichia coli* DH5 α competent cells
762 (Tsingke, TSC-C01-96). After overnight incubation at 37°C, single colonies were picked for colony
763 PCR identification. Plasmid DNA of expanded cultures was extracted (CW BIO, CW2105) after
764 verified by Sanger sequencing.

765 For protein production, heavy and light chain plasmids were co-transfected into Expi293F cells
766 (Thermo Fisher, A14527) using polyethylenimine (PEI; Yeasen, 40816ES03). The plasmid-PEI

767 complexes were prepared in sterile 0.9% NaCl solution before being added to the cell culture. The
768 transfected cells were cultured at 36.5°C with 5% CO₂ and 175 rpm shaking for 6–10 days. A
769 nutrient supplement (OPM Biosciences, F081918-001) was added to each culture at 24 hours post-
770 transfection and every 48 hours thereafter.

771 To purify the antibodies, the culture supernatant was first clarified by centrifugation (3,000 × g, 10
772 minutes). The supernatant was then incubated with Protein A magnetic beads (GenScript, L00695)
773 for 2 hours to allow antibody binding. The beads were subsequently washed, and the bound
774 antibodies were eluted using a KingFisher automated purification system (Thermo Fisher). The
775 concentration of the purified antibody was determined using a NanoDrop spectrophotometer
776 (Thermo Fisher, 840-317400), and its purity was assessed by SDS-PAGE (LabLead, P42015).

777 **RBD depletion of serum**

778 To deplete RBD-specific antibodies from serum, 50 µL of Dynabeads™ MyOne™ Streptavidin T1
779 (Invitrogen, 65601) were washed once with PBS. 10 µg of biotinylated SARS-CoV-2 Wuhan RBD
780 was incubated with the washed beads for 1 hours with gentle rotation to allow binding via
781 streptavidin-biotin interaction. The beads were then collected using a magnetic rack for 2-3 min, the
782 supernatant was discarded, and the beads were washed three times with PBS to remove unbound
783 proteins. Subsequently, 200-400 µL of serum was incubated with the RBD-conjugated beads for
784 1 hours with gentle rotation to allow specific antibody binding. Finally, the tubes were placed on the
785 magnetic rack, and the supernatant representing the RBD-depleted serum was carefully collected
786 for downstream analyses.

787 **Enzyme-linked immunosorbent assays**

788 High-binding 96-well plates (NEST, 504201) were coated overnight at 4°C with SARS-CoV-2
789 Wuhan (Sino Biological, 40592-V27H-B) or BA.5 RBD proteins (Sino Biological, 40592-V49H9-
790 B). The following day, plates were washed three times with 1×PBST (Solarbio, P1033) and blocked
791 with 250 µL 3–5% bovine serum albumin (BSA; Solarbio, A8020) in 1×PBST for 2 hours at 37°C
792 to prevent non-specific binding. After three additional washes, 100 µL of serially diluted antibodies
793 or serum samples were added to the wells and incubated for 30 minutes at room temperature.
794 Unbound antibodies were removed by five washes with 1×PBST. Subsequently, 100 µL of HRP-

795 conjugated Goat anti-Mouse IgG (H+L) Cross-Adsorbed Secondary Antibody (Invitrogen, G21040)
796 or Peroxidase AffiniPure Goat Anti-Human IgG (H+L) (Jackson ImmunoResearch, 109-035-003)
797 was added and incubated for 30 minutes at room temperature. Following a final five washes, the
798 signal was developed by adding 100 μ L of TMB substrate (Solarbio, PR1200) to each well and
799 incubating for 8 minutes in the dark. The reaction was terminated by adding 50 μ L of stop solution
800 (Solarbio, C1058). The optical density (OD) was measured at 450 nm with a reference wavelength
801 of 630 nm using a Multiskan FC microplate reader (Thermo Scientific). Final absorbance values
802 were obtained by subtracting the OD₆₃₀ reading from the OD₄₅₀ reading for each well.

803 **Surface plasmon resonance**

804 Surface plasmon resonance (SPR) experiments were conducted using a Biacore 8K+ system (Cytiva)
805 at room temperature. For competitive binding assays, His-tagged SARS-CoV-2 BA.5 RBD protein
806 (5 μ g/mL) was immobilized onto an anti-His-tagged CM5 sensor chip (Cytiva) for 1 minute.
807 Subsequently, a saturating concentration of the first antibody (Ab1, 20 μ g/mL) was injected for 2
808 minutes, immediately followed by the injection of the second antibody (Ab2, 20 μ g/mL) for another
809 2 minutes. The sensor surface was regenerated between cycles using a glycine solution (pH 1.5).
810 All binding data were recorded and processed using Biacore 8K Evaluation Software (v4.0.8.20368).
811 The degree of epitope competition was calculated using the following formula:

$$812 \quad score_{Ab2-Ab1} = 1 - \frac{response_{Ab2 \text{ after } Ab1}}{\overline{response_{Ab2 \text{ alone}}}}$$

813 Where $response_{Ab2 \text{ after } Ab1}$ represents the response units when Ab2 serves as the second
814 antibody and Ab1 as the first antibody, whereas $\overline{response_{Ab2 \text{ alone}}}$ denotes the mean response
815 units when Ab2 acts as the first antibody.

816 **DMS library construction**

817 Replicate deep mutational scanning (DMS) libraries of the SARS-CoV-2 BA.5 RBD (residues
818 N331–T531; Wuhan-Hu-1 numbering) were generated based on established protocols^{13,39} with a
819 modification. Rather than using a pooled primer mix, we performed 201 individual PCR reactions,
820 each using a specific NNS primer pair to introduce all possible amino acid substitutions at a single
821 target residue. The resulting products from each single-site mutagenesis reaction were then

822 combined to form the final comprehensive library. Each unique RBD variant was subsequently
823 tagged with a distinct 26-nucleotide (N26) barcode via PCR. The mutagenized and barcoded RBD
824 sequences were then cloned into pETcon 2649 vector and the resulted plasmid libraries were
825 amplified in electrocompetent *E. coli* DH10B cells. The association between every RBD variant and
826 its corresponding N26 barcode was established by preparing PacBio sequencing libraries and
827 performing long-read sequencing on the Sequel II platform. Amplified DMS plasmid libraries were
828 transformed into *Saccharomyces cerevisiae* strain EBY100. Transformed yeast cells were initially
829 selected on SD-CAA agar plates. Positive clones were then expanded by culturing in SD-CAA liquid
830 media. The resulting comprehensive DMS yeast libraries were preserved by flash-freezing in liquid
831 nitrogen and stored at -80 °C.

832 **Magnetic beads-based antibody mutation escape profiling**

833 High-throughput mutation escape profiling for mAbs was performed using magnetic beads based
834 on previously established protocols^{13,39}. DMS yeast libraries (Wuhan and BA.5) first underwent
835 functional pre-screening. Non-functional or misfolded RBD variants were removed using ACE2-
836 biotin conjugate (Sino Biological, 10108-H08H-B) bound to streptavidin magnetic beads (Thermo
837 Fisher, 11533D). ACE2-bound yeast cells were washed with PBS containing 0.1% (v/v) BSA,
838 released, expanded in SD-CAA liquid medium, and cryopreserved at -80°C as functional libraries.

839 For Antibody Escape Selection, thawed functional libraries were cultured overnight in SD-CAA
840 with shaking, then back-diluted into SG-CAA medium to induce RBD surface expression. Escape
841 variants of each mAb were isolated using a sequential selection strategy, with 2 rounds of negative
842 selection to deplete antibody-binding variants and 1 round of positive selection to capture the
843 antibody-escaping population using anti-c-Myc magnetic beads (Thermo Fisher, 88843). The final
844 sorted yeasts were washed, regrown overnight and subjected to plasmid extraction using a 96-well
845 kit (Coolaber, PE053). The unique N26 barcodes appended to each RBD variant were amplified by
846 PCR using extracted plasmid as template. PCR products were purified with Ampure XP beads
847 (Beckman Coulter, A63882) and subjected to high-throughput single-end sequencing (NextSeq
848 500/550 platforms or MGI200 platforms).

849 **Antibody DMS data analysis**

850 The raw sequencing data from the DMS were processed as previously described¹³. Specifically, the
851 barcode sequences detected from both the antibody-screened and reference libraries were aligned
852 with a barcode-variant dictionary derived from PacBio sequencing data of the Wuhan and BA.5
853 DMS libraries using the alignparse (v.0.6.2) and dms_variants (v.1.4.3) tools. Ambiguous barcodes
854 were excluded during the merging of yeast libraries. Only barcodes detected more than five times
855 in the reference library were considered for further analysis. The escape score for a variant X,
856 present in both the screened and reference libraries, was calculated as $F \times (n_{X,ab}/N_{ab}) / (n_{X,ref}/N_{ref})$,
857 where F is a scaling factor to normalize the scores to a 0–1 range, and n and N represent the numbers
858 of detected barcodes for variant X and the total barcodes in the antibody-screened (ab) or reference
859 (ref) samples, respectively. For antibodies subjected to DMS with multiple replicates using different
860 mutant libraries, the final escape score for each mutation was averaged for subsequent analyses.

861 We used graph-based unsupervised clustering and embedding to assign an epitope group to each
862 antibody and visualize them in a two-dimensional space. Initially, site escape scores (sum of
863 mutation escape scores per residue) for each antibody were normalized to a sum of one, representing
864 a distribution over RBD residues. The dissimilarity between two antibodies is defined based on the
865 Pearson's correlation coefficient of their escape score vectors using numpy (v1.25.2). A k-nearest-
866 neighbour graph was constructed using the python-igraph module (v.0.9.6), and Leiden clustering
867 was applied to assign a cluster to each antibody⁵⁴. Cluster names were manually annotated on the
868 basis of the characteristic sites in the average escape profiles of each cluster, using the same
869 nomenclature as our previously published DMS dataset¹³. To visualize the dataset in two
870 dimensions, uniform manifold approximation and projection was performed based on the k-nearest-
871 neighbour graph using umap-learn module (v.0.5.2), and figures were generated using R package
872 ggplot2 (v.3.3.3).

873 To compute the average immune pressure or identify escape hotspots using a collection of mAb
874 DMS profiles, we incorporating two types of weight to account for the impact of each mutation on
875 neutralizing activity and codon constraints at each residue. For codon usage constraints, mutations
876 inaccessible through single nucleotide changes were assigned a weight of zero, whereas others
877 received a weight of 1.0. We used Wuhan/D614G (Wuhan-Hu-1 reference genome) and BA.4/5
878 (EPI_ISL_11207535) to define one-nucleotide-accessible amino acid mutations. Neutralizing

879 activity weights were calculated as $-\log_{10}(\text{IC}_{50})$, with IC_{50} values below 0.0005 or above 1.0
880 adjusted to 0.0005 or 1.0, respectively. Raw escape scores for each antibody were normalized by
881 the maximum score across all mutants. The weighted score for each antibody and mutation was
882 obtained by multiplying the normalized scores by the corresponding two weights, and the final
883 mutation-specific weighted score was the sum of scores for all antibodies in the designated set,
884 subsequently normalized to a 0–1 range. To visualize the calculated escape maps, sequence logos
885 were generated using the Python module logomaker (v.0.8).

886

887 **Figure legends**

888 **Figure 1 | mRNA and inactivated vaccine priming induce distinct levels of immune imprinting.**

889 **a**, Schematic of the SARS-CoV-2-related immune histories and sampling time of the inactivated-
890 only and mRNA-vaccinated cohorts involved in this study. **b**, Representative flow cytometry dot
891 plots of cross-reactive memory B cells from the inactivated-only (top) and mRNA-vaccinated
892 (bottom) cohorts. APC, allophycocyanin; PE, phycoerythrin; BV421, Brilliant Violet 421. **c**, Scatter
893 plots showing the proportion of cross-reactive memory B cells (left), JN.1-reactive memory B cells
894 (middle), and Wuhan-reactive memory B cells (right). **d**, Serum IgG midpoint titre against Wuhan
895 (left) or JN.1 (right) RBD before and after Wuhan RBD depletion. Statistical significance of the
896 fold-reduction in titres was assessed between two cohorts. Dashed lines indicate the limit of
897 detection (midpoint titre = 10). **e**, NAb response of the two cohorts against a panel of SARS-CoV-2
898 variant pseudoviruses. Geometric mean titres (GMTs) are shown on the top. Dashed lines indicate
899 the limit of detection ($NT_{50} = 10$). **f**, Frequency of heavy chain V gene usage of the two cohorts.
900 IGHV3-53 and IGHV3-66 were combined for analysis. Two-tailed Wilcoxon rank-sum tests were
901 used in **c-e**. * $P < 0.05$, ** $P < 0.01$, *** $P < 0.001$, **** $P < 0.0001$; NS, not significant ($P > 0.05$).

902 **Figure 2 | V(D)J-humanized mice recapitulate severe SARS-CoV-2 imprinting.**

903 **a**, Schematic of the immunization regimen and sampling timeline for wild-type and V(D)J-
904 humanized mice. The number of mice is indicated at the time point for each endpoint experiment.
905 **b**, Scatter plots showing the proportion of cross-reactive memory B cells in draining lymph nodes
906 of the two mouse strains after one (left) or two (right) BA.5 boosts. **c**, Serum IgG midpoint titre of
907 the two mouse strains after one (left) or two (right) BA.5 boosts against Wuhan or BA.5 RBD before
908 and after Wuhan RBD depletion. Statistical significance of the fold-reduction in titres was assessed
909 between humanized and wild-type mice. Dashed lines indicate the limit of detection (midpoint
910 titre = 100). **d**, Serum neutralization titres (NT_{50}) of the two mouse models after Wuhan priming
911 (left), one BA.5 boost (middle), or two BA.5 boosts (right) against a panel of SARS-CoV-2 variant
912 pseudoviruses. Geometric mean titres (GMTs) are shown on the top. Dashed lines indicate the limit
913 of detection ($NT_{50} = 60$). Two-tailed Wilcoxon rank-sum tests were used in **b-d**.

914 **Figure 3 | Distinct antibody landscapes between mRNA vaccinated humanized and wild-type**

915 **mice.**

916 **a–c**, Normalized average DMS escape scores for mAbs isolated from humanized (top) and wild-
917 type (bottom) mice following Wuhan priming (**a**), the first BA.5 booster (**b**), or the second BA.5
918 booster (**c**). Escape scores were aggregated and weighted by the IC_{50} of each individual mAb (To
919 focus on the neutralizing mAbs, lower IC_{50} corresponds to greater weight) against D614G for
920 Wuhan-primed groups or BA.5 for BA.5-boosted groups. Codon constraints were applied (see
921 Methods). In each panel, the ten residues with the highest cumulative escape scores are annotated,
922 with their specific mutational escape profiles visualized as logo plots above the scatter plots. To
923 highlight divergent immune pressure, residues exhibiting pronounced differences between
924 humanized and wild-type strains (as identified in Extended Data Fig. 6) are colored red in both the
925 scatter plots and logo plots.

926

927 **Figure 4 | V(D)J germline difference shapes vaccination- induced SARS-CoV-2 antibody**
928 **epitope distribution.**

929 Epitope distribution of the antibody repertoire generated after Wuhan priming in humanized (**a**) and
930 wild-type mice (**b**). The Wuhan RBD structure (PDB: 6m0j) is displayed as a surface map colored
931 by normalized aggregate escape scores, with major epitope groups outlined in distinct colors. Their
932 neutralizing category, antibody count, and percentage are indicated. Neutralizing category is
933 classified based on geometric mean of IC_{50} : Strong neutralizing ($<0.1 \mu\text{g/mL}$), Neutralizing ($0.1 \leq$
934 $IC_{50} < 1 \mu\text{g/mL}$), and Weak neutralizing ($1 \leq IC_{50} \leq 10 \mu\text{g/mL}$). Epitope groups accounting for $<5\%$
935 of the total antibodies are not labeled. Key escape residues for each group are displayed as logos,
936 and the sites with the highest escape scores per group are labeled on the structure. Paired heavy and
937 light chain V-gene usage for each epitope is shown in Sankey plots. **c**, Pyramidal bar charts showing
938 the proportional distribution of epitope groups in antibodies isolated from humanized and wild-type
939 mice after Wuhan priming and after one or two BA.5 boosts. Bars are colored according to the \log_{10}
940 geometric mean IC_{50} of antibodies within each group.

941 **Figure 5 | IGHV3-53/66-encoded Class 1 antibody drives SARS-CoV-2 imprinting through**
942 **epitope masking.**

943 **a**, Donut plots showing the cross-reactivity of A1 antibodies from humanized or wild-type mice.
944 The number of antibodies are indicated in the centre of the donut. Antibodies exhibiting ELISA
945 OD450 values > 2 against both WT and BA.5 RBDs (1 $\mu\text{g}/\text{mL}$) were defined as cross-reactive.
946 Those showing an OD450 > 2 for one variant but < 2 for the other were classified as specific. **b**,
947 Heatmap of competitive SPR for various antibody groups. The definition of the competition score
948 is described in the Methods section. **c**, Schematic of the molecular mechanism by which pre-existing
949 IGHV3-53/66-encoded A1 antibodies cause strong immune imprinting. **d**, Schematic of the
950 antibody passive transfer experiment. Timing of mRNA vaccinations, antibody injection, blood
951 collection, and FACS analysis are indicated. Mice were divided into experimental groups (receiving
952 400 μg BD55-1205-hIgG1, 200 μg BD55-1205-hIgG1, or 200 μg BD55-1205-mIgG1) and control
953 groups (receiving 200 μg BD57-2665-mIgG1 or PBS). The number of mice per group is indicated
954 at the endpoint. **e**, DMS escape map logoplots for BD55-1205 and BD57-2665 and their projection
955 onto the SARS-CoV-2 Wuhan RBD (PDB: 6m0j). **f**, Scatter plots showing the proportion of cross-
956 reactive memory B cells in draining lymph nodes after one (left) or two (right) BA.5 boosts. **g**,
957 Scatter plots showing the proportion of cross-reactive germinal center B cells in draining lymph
958 nodes after one BA.5 boost. **h**, Serum IgG midpoint titre against BA.5 RBD before and after Wuhan
959 RBD depletion. Statistical significance of the fold-reduction in titres was assessed between groups.
960 Dashed lines indicate the limit of detection (midpoint titre = 100). Two-tailed Wilcoxon rank-sum
961 tests were used in **f-h**.

962 **Figure 6 | IGHV3-53 knock-in mice faithfully reflect SARS-CoV-2 antibody map in human.**

963 **a**, Usage percentage of IGHV3-53 and Ighv3-1 in naïve B cells from HTGTS sequencing of IGHV3-
964 53^{+/+} (balb/c), IGHV3-53^{+/-} (balb/c* C57B6/J), and wild-type (C57B6/J) mice. **b**, Schematic of the
965 immunization regimen and time points for blood collection and FACS analysis of the three mouse
966 models involved in this study. The number of mice is indicated above the timeline. **c**, Scatter plots
967 showing the proportion of cross-reactive memory B cells in draining lymph nodes of the three mouse
968 models after two BA.5 boosts. **d**, Serum IgG midpoint titre of the three mouse strains after two BA.5
969 boosts against BA.5 RBD before and after Wuhan RBD depletion. Statistical significance of the
970 fold-reduction in titres was assessed between groups. Dashed lines indicate the limit of detection
971 (midpoint titre = 100). **e**, Serum neutralization titres (NT₅₀) of the three mouse strains after one (left)

972 or two (right) BA.5 boosts against a panel of SARS-CoV-2 variant pseudoviruses. Geometric mean
973 titres (GMTs) are shown on the top. Dashed lines indicate the limit of detection ($NT_{50} = 60$). **f**,
974 Schematic of the immunization regimen simulating real-world SARS-CoV-2 exposure history. **g**,
975 Serum neutralization titres (NT_{50}) of IGHV3-53^{+/+} and wild-type mice against a panel of SARS-
976 CoV-2 variant pseudoviruses. Geometric mean titres (GMTs) are shown on the top. Dashed lines
977 indicate the limit of detection ($NT_{50} = 180$). **h**, Antigenic cartography was performed using mouse
978 (top) and human (bottom) serum neutralization data. Each square indicates a serum sample, and
979 each circle indicates a SARS-CoV-2 variant. Two-tailed Wilcoxon rank-sum tests were used in **c-e**
980 and **g**.

981 **Extended Data Figure 1 | Different epidemiological landscape of XFG and NB.1.8.1 in 2025.**

982 **a**, Prevalence of XFG and NB.1.8.1 in China and the rest of the world as of October 5, 2025. The
983 asterisk (*) denotes the specific lineage and its sublineages. Data were retrieved from CovSpectrum
984 (<https://cov-spectrum.org/>).

985 **Extended Data Figure 2 | Enrichment of IGHV3-53/66 and high SHM rate characterize the**
986 **mRNA-imprinted antibody repertoire.**

987 **a**, Clonal analysis of memory B cells from individuals in the mRNA-vaccinated cohort. Single
988 clones are colored white. The numbers of B cells analyzed are labelled in the centre of the donut
989 plots. **b**, Paired heavy and light chain V-gene usage for memory B cells from the mRNA-vaccinated
990 and inactivated-only cohorts. **c**, **d**, Violin plots comparing somatic hypermutation (SHM) rates
991 between the two cohorts, shown for heavy and light chains (**c**) and representative heavy chain V-
992 genes (**d**). The number of sequences (n) is indicated above each plot. Two-tailed Wilcoxon rank-
993 sum tests were used in **d**.

994 **Extended Data Figure 3 | V(D)J-humanized mice exhibit a cellular imprinting phenotype**
995 **dominated by cross-reactive GC and memory B cells.**

996 **a-c**, Scatter plots showing the proportion of cross-reactive GC B cells (**a**), total GC B cells (**b**),
997 and class-switched memory B cells (**c**). The indicated percentages reflect the frequency relative to
998 their respective parental gates defined in Supplementary Information Fig. 1b.

999 **Extended Data Figure 4 | Repeated Omicron boosters fail to elicit robust Omicron-specific**
1000 **neutralization in imprinted humanized mice.**

1001 **a**, Line plots showing longitudinal pseudovirus neutralization titres (NT₅₀) against a panel of
1002 SARS-CoV-2 variants in paired humanized and wild-type mice across Wuhan priming and BA.5
1003 booster timepoints; lines connect data from the same mouse. Dashed lines indicate the limit of
1004 detection (NT₅₀ = 60). Two-tailed Wilcoxon rank-sum tests were used.

1005 **Extended Data Figure 5 | Neutralization potency and cross-reactivity of mAbs from**
1006 **humanized and wild-type mice.**

1007 **a,b**, Comparison of antibody IC₅₀ values against D614G and BA.5(**a**) and cross-reactivity
1008 proportion (**b**) from humanized and wild-type mice. Two-tailed Wilcoxon rank-sum tests were
1009 used in **a**. Antibodies exhibiting ELISA OD450 values > 2 against both WT and BA.5 RBDs (1
1010 µg/mL) were defined as cross-reactive. Those showing an OD450 > 2 for one variant but < 2 for
1011 the other were classified as specific.

1012 **Extended Data Figure 6 | Differential escape hotspots in humanized versus wild-type mice.**

1013 **a–c**, Scatter plots comparing the normalized average DMS escape scores of neutralizing
1014 antibodies isolated from humanized (x-axis) versus wild-type (y-axis) mice following Wuhan
1015 priming (**a**), the first BA.5 booster (**b**), and the second BA.5 booster (**c**). Residues falling along the
1016 diagonal (y=x) indicate shared immune pressure between the two models. To identify divergent
1017 hotspots—including those with low-to-moderate scores in one strain that are absent in the other—
1018 a shaded tolerance region was defined by the boundaries $y = 1.4x + 0.3$ and $y = 0.6x - 0.18$. Points
1019 falling outside this shaded region represent distinct escape hotspots. Among these outliers, the five
1020 residues with the highest escape scores in each group are highlighted in red. Related to Fig. 3.

1021 **Extended Data Figure 7 | Distinct SARS-CoV-2 antibody epitope distribution after**
1022 **sequential BA.5 boosts.**

1023 **a-d**, Epitope distribution of the antibody repertoire generated after one BA.5 boost (**a, b**) or two

1024 BA.5 boosts (**c, d**) in humanized mice (**a, c**) and wild-type mice (**b, d**). Related to Figure 4. **e**,
1025 Pyramidal bar charts showing the proportional distribution of epitope groups in antibodies isolated
1026 from humanized and wild-type mice after one or two BA.5 boosts. Bars are colored according to
1027 the log₁₀ geometric mean IC₅₀ of antibodies within each group.

1028 **Extended Data Figure 8 | Pharmacokinetics and dose-dependent suppressive effects of**
1029 **antibodies used in passive transfer.**

1030 **a**, Schematic of the *in vivo* monoclonal antibody pharmacokinetic study. **b**, Serum IgG titres over
1031 time following antibody injection (mIgG1 forms were detected using an anti-mouse Fc secondary
1032 antibody, and hIgG1 forms using an anti-human Fc secondary antibody). Dashed lines indicate the
1033 limit of detection (midpoint titre = 100). **c**, Schematic of the BD55-1205 dose-ranging experiment.
1034 **d**, Corresponding serum IgG titres before and after Wuhan RBD depletion. Statistical significance
1035 of the fold-reduction in titres was assessed between groups. Dashed lines indicate the limit of
1036 detection (midpoint titre = 100). Two-tailed Wilcoxon rank-sum tests were used in **d**.

1037 **Extended Data Figure 9 | IGHV3-53 knock-in mice exhibit diminished Omicron**
1038 **neutralization boosting compared to wild-type mice.**

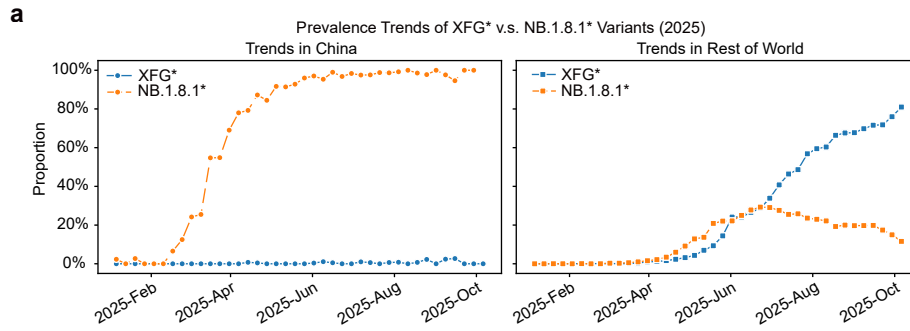
1039 **a**, Line plots showing longitudinal pseudovirus neutralization titres (NT₅₀) against a panel of
1040 SARS-CoV-2 variants in paired IGHV3-53^{+/+} (top), IGHV3-53^{+/-} (middle), and wild-type (bottom)
1041 mice across BA.5 booster timepoints; lines connect data from the same mouse. Dashed lines
1042 indicate the limit of detection (NT₅₀ = 60). Two-tailed Wilcoxon rank-sum tests were used.

1043 **Extended Data Figure 10 | Strong back-boosting of Wuhan immunity in IGHV3-53 KI mice**
1044 **restricts the breadth of neutralization against emerging variants.**

1045 **a**, Serum neutralization titres (NT₅₀) of IGHV3-53^{+/+} and wild-type mice against a panel of SARS-
1046 CoV-2 variant pseudoviruses following the fifth dose (XBB.1.5). Geometric mean titres (GMTs) are
1047 shown on the top. Dashed lines indicate the limit of detection (NT₅₀ = 180). **b**, Radar plot illustrating
1048 the back-boosting effect of the JN.1 booster on neutralization titres against pre-JN.1 variants. **c**,
1049 Neutralization profiles of IGHV3-53^{+/+} and wild-type mice following XBB.1.5 and JN.1 boosters.

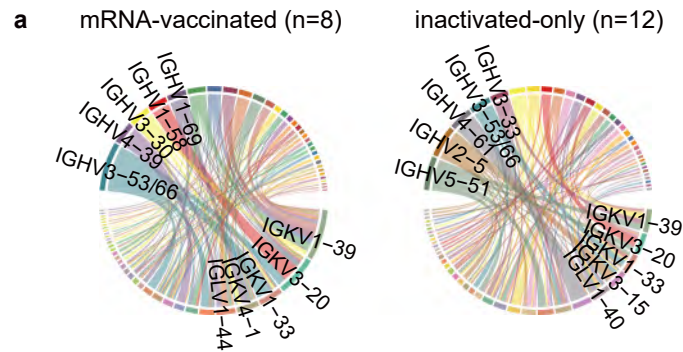
1050 Fold changes and statistical significance between highlighted variants are indicated. Lines connect
1051 data from the same mouse. Two-tailed Wilcoxon rank-sum tests were used in **a-c**.

Extended Data figure 1



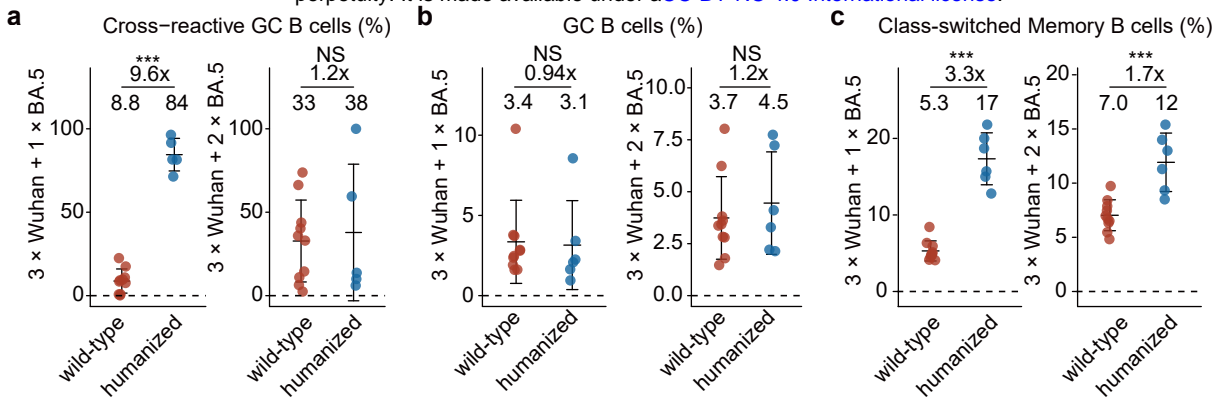
Extended Data Figure 1 | Different epidemiological landscape of XFG and NB.1.8.1 in 2025.
a, Prevalence of XFG and NB.1.8.1 in China and the rest of the world as of October 5, 2025. The asterisk (*) denotes the specific lineage and its sublineages. Data were retrieved from CovSpectrum (<https://cov-spectrum.org/>).

Extended Data figure 2



Extended Data Figure 2 | Paired heavy and light chain V-gene usage for human memory B cells
a, Paired heavy and light chain V-gene usage for memory B cells from the mRNA-vaccinated and inactivated-only cohorts.

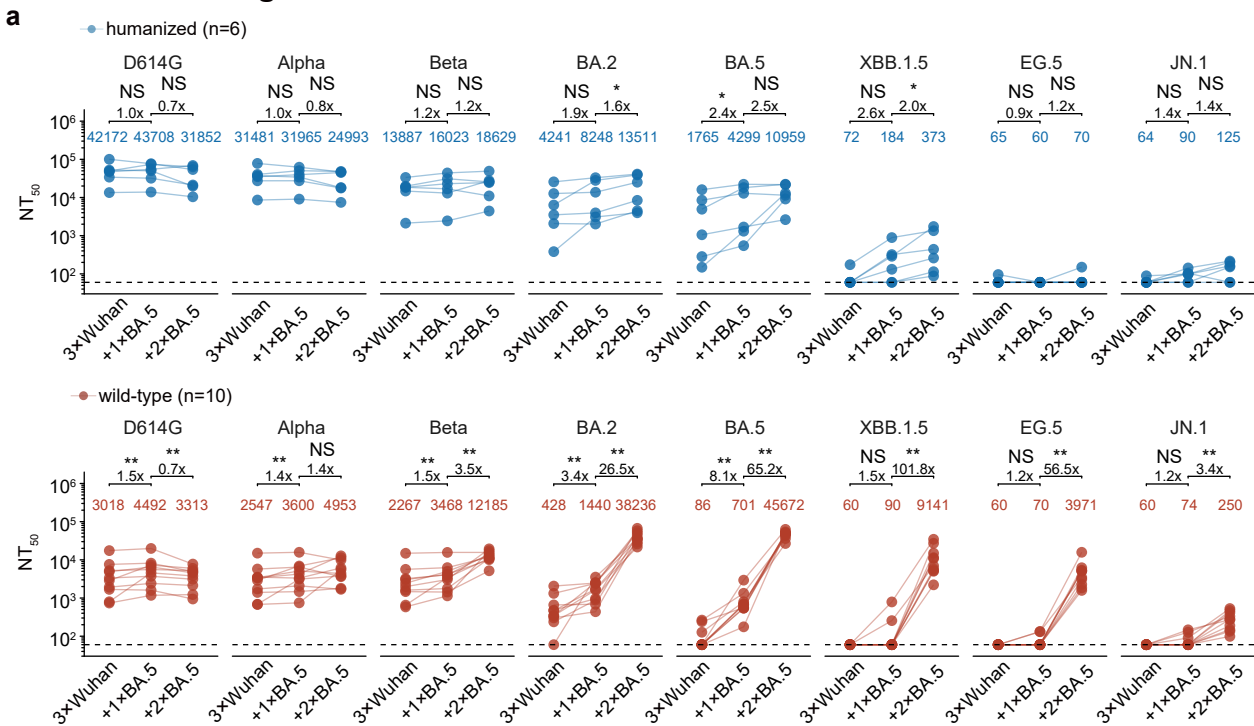
Extended Data Figure 3



Extended Data Figure 3 | V(D)J-humanized mice exhibit a cellular imprinting phenotype dominated by cross-reactive GC and memory B cells.

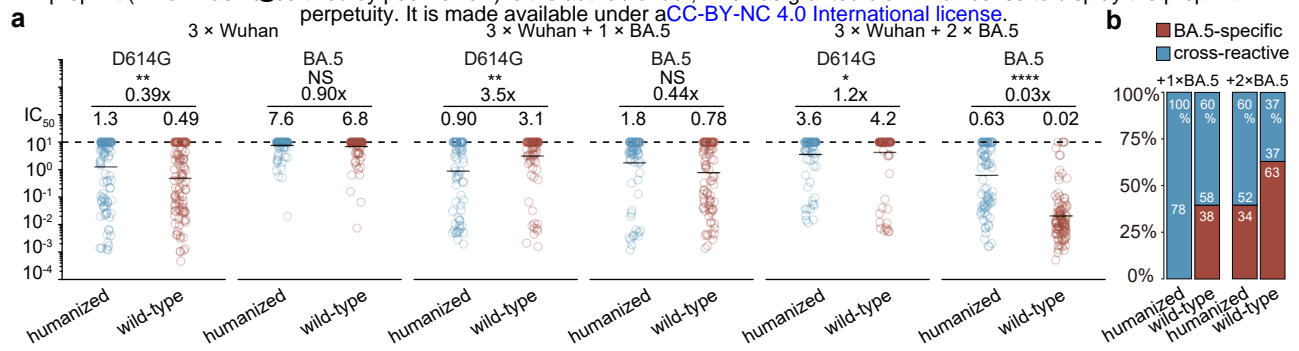
a-c, Scatter plots showing the proportion of cross-reactive GC B cells (a), total GC B cells (b), and class-switched memory B cells (c). The indicated percentages reflect the frequency relative to their respective parental gates defined in Supplementary Information Fig. 1b.

Extended Data figure 4



Extended Data Figure 4 | Repeated Omicron boosters fail to elicit robust Omicron-specific neutralization in imprinted humanized mice.

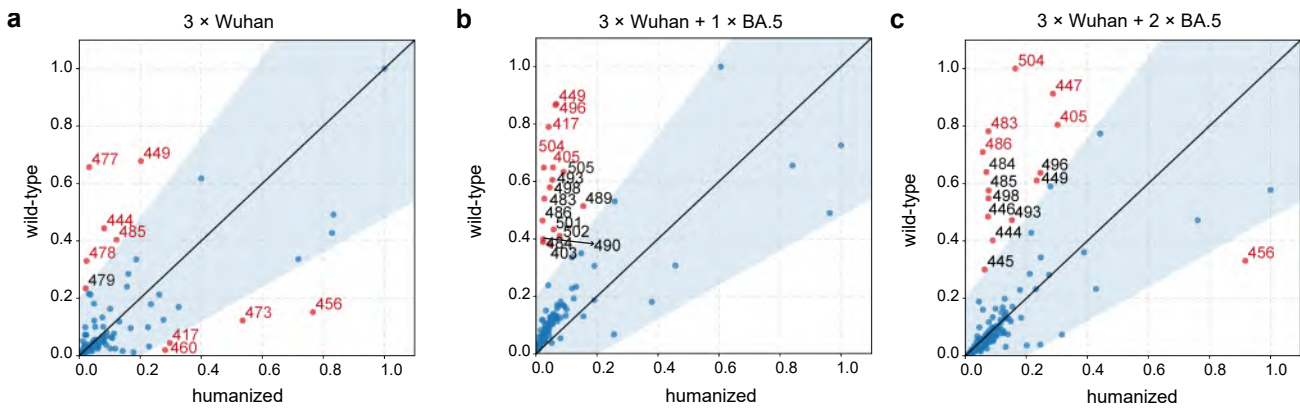
a, Line plots showing longitudinal pseudovirus neutralization titres (NT_{50}) against a panel of SARS-CoV-2 variants in paired humanized and wild-type mice across Wuhan priming and BA.5 booster timepoints; lines connect data from the same mouse. Dashed lines indicate the limit of detection ($NT_{50} = 60$). Two-tailed Wilcoxon rank-sum tests were used.



Extended Data Figure 5 | Neutralization potency and cross-reactivity of mAbs from humanized and wild-type mice.

a,b. Comparison of antibody IC_{50} values against D614G and BA.5(a) and cross-reactivity proportion (b) from humanized and wild-type mice. Two-tailed Wilcoxon rank-sum tests were used in a. Antibodies exhibiting ELISA OD450 values > 2 against both WT and BA.5 RBDs (1 μ g/mL) were defined as cross-reactive. Those showing an OD450 > 2 for one variant but < 2 for the other were classified as specific.

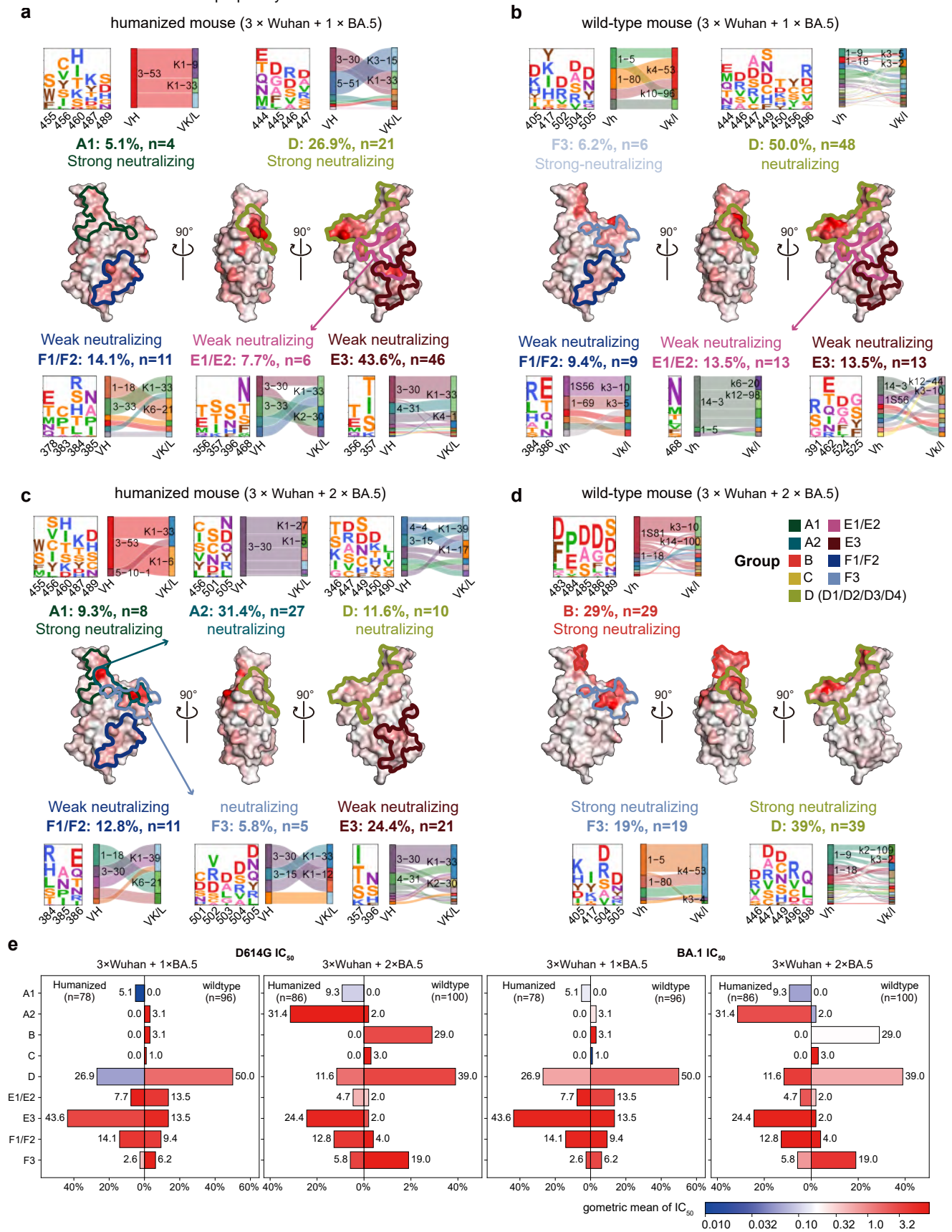
Extended Data figure 6



Extended Data Figure 6 | Differential escape hotspots in humanized versus wild-type mice.

a–c. Scatter plots comparing the normalized average DMS escape scores of neutralizing antibodies isolated from humanized (x-axis) versus wild-type (y-axis) mice following Wuhan priming (a), the first BA.5 booster (b), and the second BA.5 booster (c). Residues falling along the diagonal ($y=x$) indicate shared immune pressure between the two models. To identify divergent hotspots—including those with low-to-moderate scores in one strain that are absent in the other—a shaded tolerance region was defined by the boundaries $y = 1.4x + 0.3$ and $y = 0.6x - 0.18$. Points falling outside this shaded region represent distinct escape hotspots. Among these outliers, the five residues with the highest escape scores in each group are highlighted in red. Related to Fig. 3.

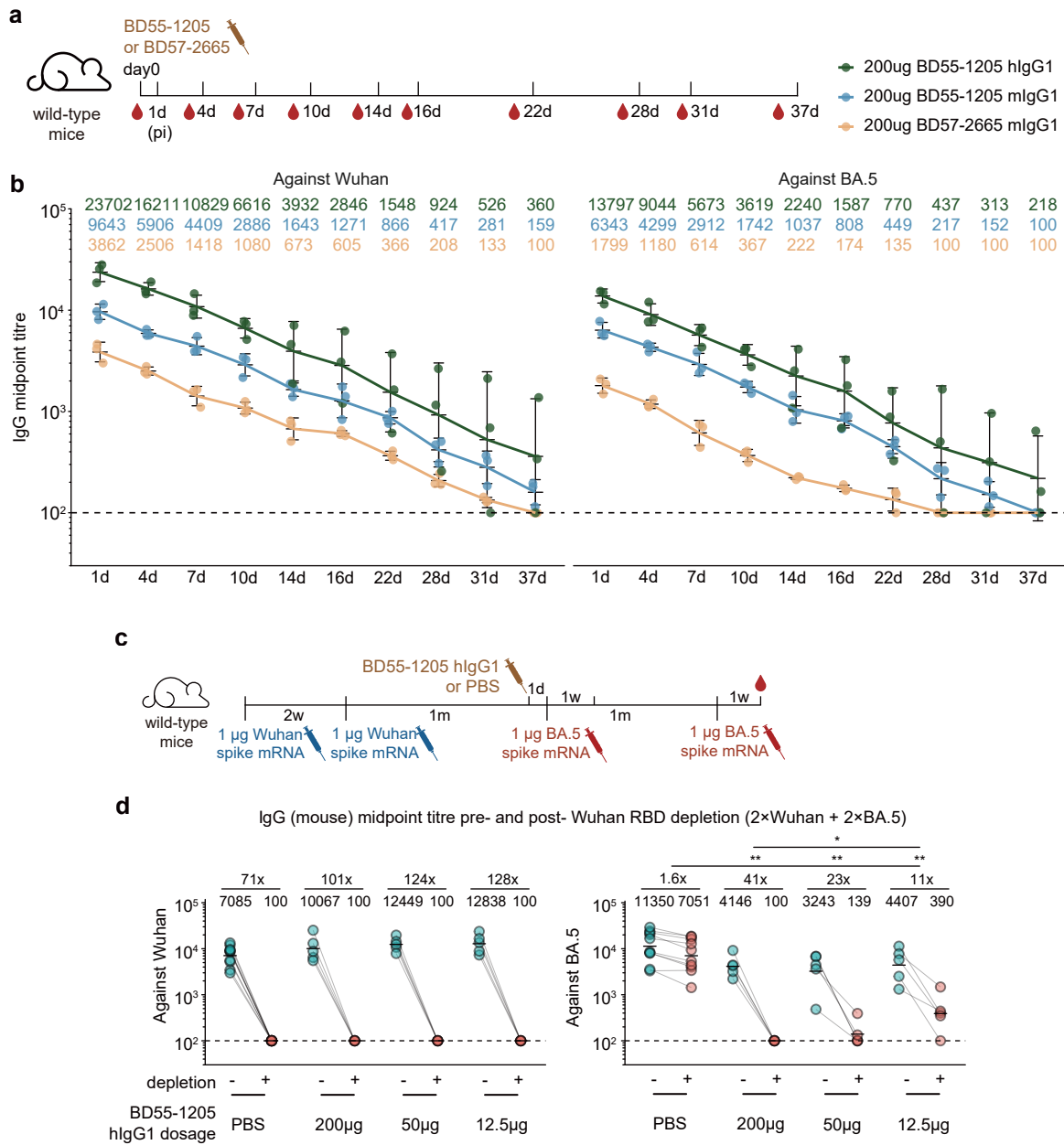
Extended Data figure 7



Extended Data Figure 7 | Distinct SARS-CoV-2 antibody epitope distribution after sequential BA.5 boosts.

a-d, Epitope distribution of the antibody repertoire generated after one BA.5 boost (a, b) or two BA.5 boosts (c, d) in humanized mice (a, c) and wild-type mice (b, d). Related to Figure 4. e, Pyramidal bar charts showing the proportional distribution of epitope groups in antibodies isolated from humanized and wild-type mice after one or two BA.5 boosts. Bars are colored according to the \log_{10} geometric mean IC_{50} of antibodies within each group.

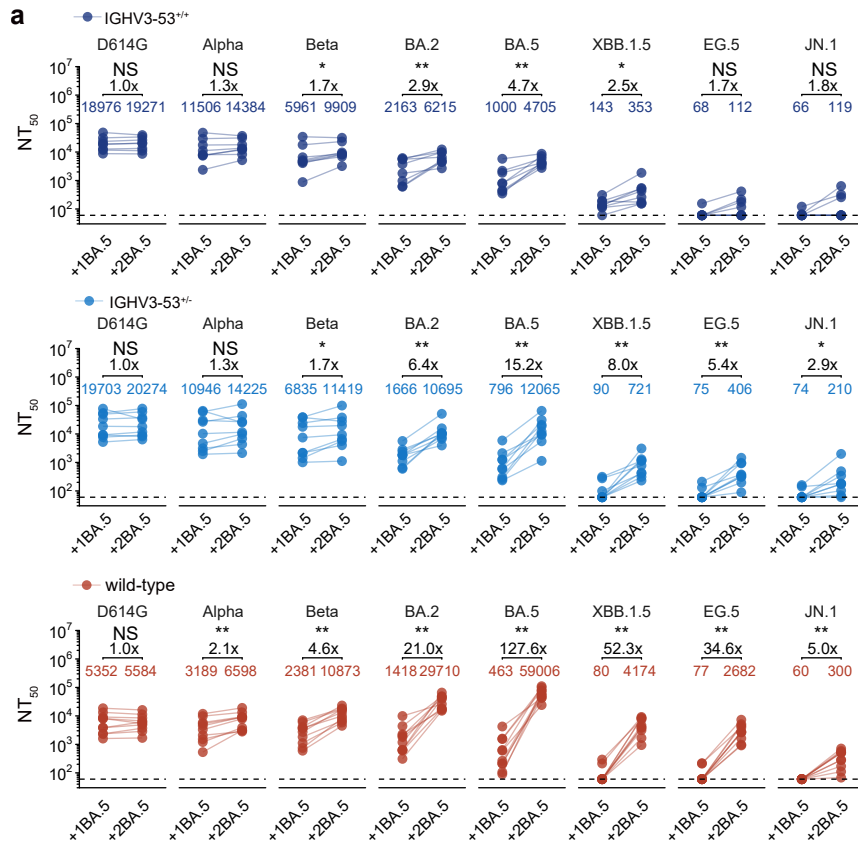
Extended Data figure 8



Extended Data Figure 8 | Pharmacokinetics and dose-dependent suppressive effects of antibodies used in passive transfer.

a, Schematic of the in vivo monoclonal antibody pharmacokinetic study. b, Serum IgG titres over time following antibody injection (mIgG1 forms were detected using an anti-mouse Fc secondary antibody, and hlgG1 forms using an anti-human Fc secondary antibody). Dashed lines indicate the limit of detection (midpoint titre = 100). c, Schematic of the BD55-1205 dose-ranging experiment. d, Corresponding serum IgG titres before and after Wuhan RBD depletion. Statistical significance of the fold-reduction in titres was assessed between groups. Dashed lines indicate the limit of detection (midpoint titre = 100). Two-tailed Wilcoxon rank-sum tests were used in d.

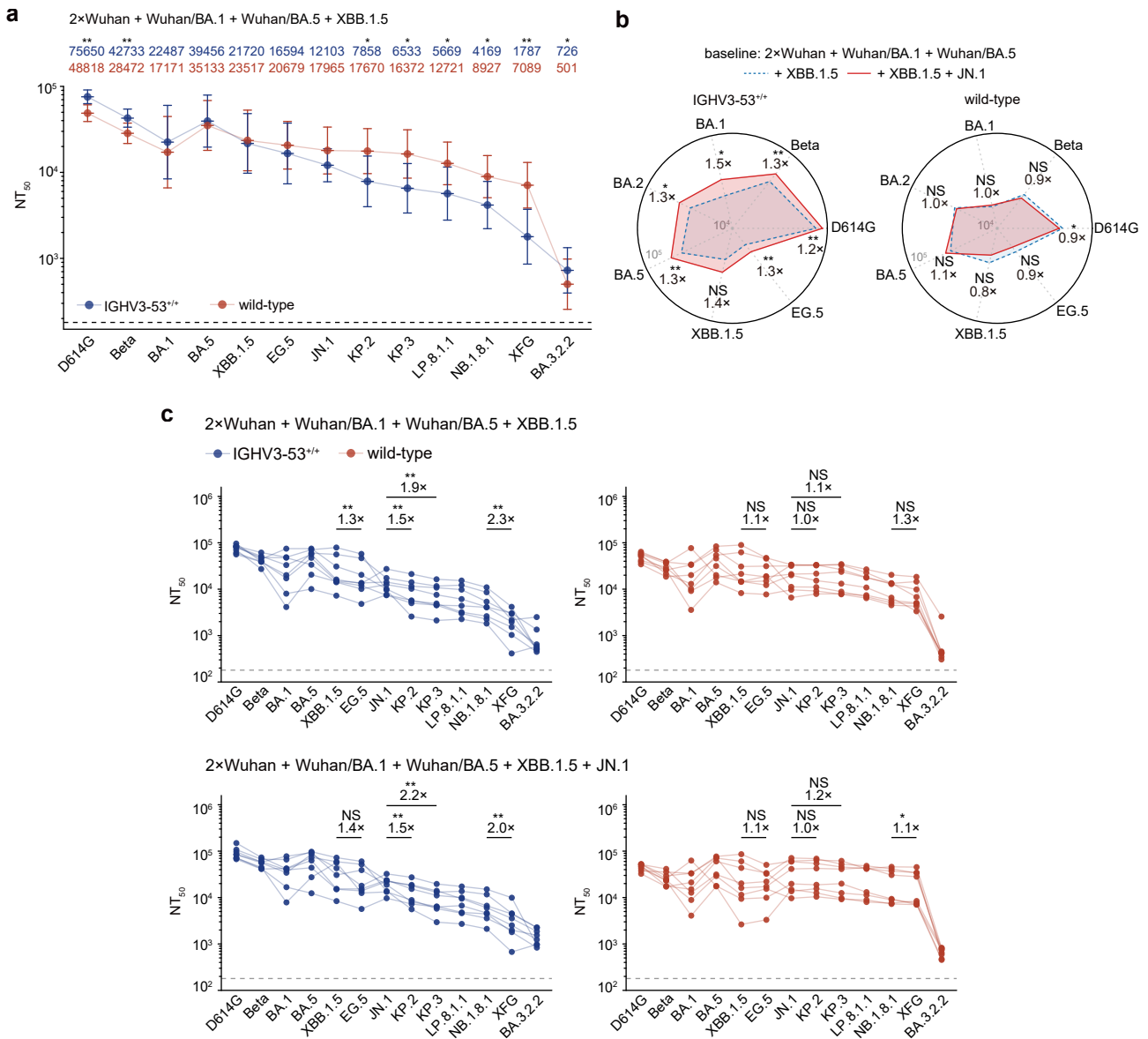
Extended Data Figure 9



Extended Data Figure 9 | IGHV3-53 knock-in mice exhibit diminished Omicron neutralization boosting compared to wild-type mice.

a, Line plots showing longitudinal pseudovirus neutralization titres (NT_{50}) against a panel of SARS-CoV-2 variants in paired IGHV3-53^{+/+} (top), IGHV3-53^{-/-} (middle), and wild-type (bottom) mice across BA.5 booster timepoints; lines connect data from the same mouse. Dashed lines indicate the limit of detection ($NT_{50} = 60$). Two-tailed Wilcoxon rank-sum tests were used.

Extended Data Figure 10



Extended Data Figure 10 | Strong back-boosting of Wuhan immunity in IGHV3-53 KI mice restricts the breadth of neutralization against emerging variants.

a, Serum neutralization titres (NT_{50}) of IGHV3-53+/+ and wild-type mice against a panel of SARS-CoV-2 variant pseudoviruses following the fifth dose (XBB.1.5). Geometric mean titres (GMTs) are shown on the top. Dashed lines indicate the limit of detection ($NT_{50} = 180$). b, Radar plot illustrating the back-boosting effect of the JN.1 booster on neutralization titres against pre-JN.1 variants. c, Neutralization profiles of IGHV3-53+/+ and wild-type mice following XBB.1.5 and JN.1 boosters. Fold changes and statistical significance between highlighted variants are indicated. Lines connect data from the same mouse. Two-tailed Wilcoxon rank-sum tests were used in a-c.